DIAGNOSIS OF ARCING IN RETAINING RINGS OF
TURBOGENERATORS

BY

SAJAL KUMAR HARMUKH

THESIS

Submitted in partial fulfillment of the requirements
for the degree of Master of Science in Electrical and Computer Engineering
in the Graduate College of the
University of Illinois at Urbana-Champaign, 2016

Urbana, Illinois

Adviser:

Associate Professor Kiruba Sivasubramaniam Haran

ABSTRACT

Retaining rings are an important and most highly stressed component of the entire turbogenerator system. Arcing in retaining rings is a very serious problem and could easily escalate to a full–blown failure. In this project we diagnose arcing in the retaining rings. We determine the most likely mechanism by which arcing occurs and the category of events which lead to it. Specifically, we try to test two different mechanisms which could have led to the arc marks. The first one is sparking due to high field effects (or high voltage gradient across the contact junction) and the other is a make-and-break contact arcing owing to the presence of inductance in the system. Experiments performed to measure the contact resistance between the retaining ring and mild iron piece indicate that even very high fault currents cannot produce the voltage required to cause sparking. Transient 3-D finite element simulations show that a make-and-break contact can generate localized voltage spikes, on account of small contact break, which are high enough to lead to arcing. Interestingly this can happen at relatively low currents.

To my parents, for their love and support.

ACKNOWLEDGMENTS

Though only my name appears on the cover of this thesis, a great many people have contributed to its production. I owe my gratitude to all those people who have made this dissertation possible and because of whom my graduate experience has been one that I will cherish forever.

I would like to express my deepest gratitude to Professor Kiruba Sivasubramaniam Haran for his encouragement, guidance, and support throughout this research process, without which this work would not have been possible. I have been amazingly fortunate to have an advisor who gave me the freedom to explore on my own, and at the same time the guidance to recover when my steps faltered. Always teeming with brilliant ideas and witty comments, Prof Kiruba has been a phenomenal collaborator and an inspirational mentor.

I would like to thank Professor James Phillips from the Department of Aerospace Engineering for his time and help with the compressive test machine in Talbot Laboratory.

I would also like to thank Kevin James Colravy for his valuable time and help in the power research laboratory.

I am grateful to the ECE Machine Shop staff for helping me out with the hardware. Their timely work was the reason that a lot of hardware experiments could have been performed.

The post–processing of the specimens, including surface profilometry and chemical characterization, was carried out in part in the Frederick Seitz Materials Research Laboratory Central Research Facilities, University of Illinois. I am deeply grateful to them for allowing me to use the state–of–the–art testing and characterization equipment.

I deeply thank my close friend and also my research teammate, Andy Yoon, who always took time from his busy schedule to help me with my queries regarding simulation and hardware; without his help this work would have been significantly delayed. I would also like to thank Jon Martin, Christo-

TABLE OF CONTENTS

CHAPTER 1

INTRODUCTION

The motivation behind this work stems from the surveys done by EPRI to evaluate the performance of newly installed 18 Mn-18 Cr retaining rings nearly a decade ago. The survey identified arcing as the principal damage mechanism for the retaining rings of turbogenerators. Arcing is an undesirable phenomenon as it can quickly progress to full–scale damage in the highly stressed retaining rings. In this project we diagnose how arcing occurs and explore the events leading to it.

1.1 Retaining Rings

In a synchronous turbogenerator the rotor windings sit inside the slots machined on rotor forging and are supported by wedges, which prevent the windings from moving out when the machine is rotating at high speeds. However, at either rotor end these windings have to make a turn to go back into the slots on the other side and wedges cannot be inserted at these locations. These end turns (or end windings) are thus unprotected against very high centrifugal forces. To hold these end windings against these forces, steel based alloys called retaining rings are used to keep them in place. In addition, the rings also provide a path for any circulating current that may flow on the rotor surface. Figure 1.1 shows the image of a retaining ring. The castellations on the inner edge are required to inhibit any axial movement of the ring on the rotor forging.

There are two retaining rings for the two ends - turbine end and exciter end - of the generator rotor. Figure 1.2 shows the location of the retaining rings on a rotor. The inner diameter of the rings is smaller than the outer diameter of the rotor forging on which the rings are to be mounted. The rings are expanded by heating and mounted onto the forging. The rings then

Figure 1.1: Image of retaining ring with castellations for axial restraint. [1]

"shrink" on the forging when they cool down. Such a fit is called a "shrink fit" or an "interference fit" and the surface of rotor forging in contact with retaining ring is called the shrink-fit region.
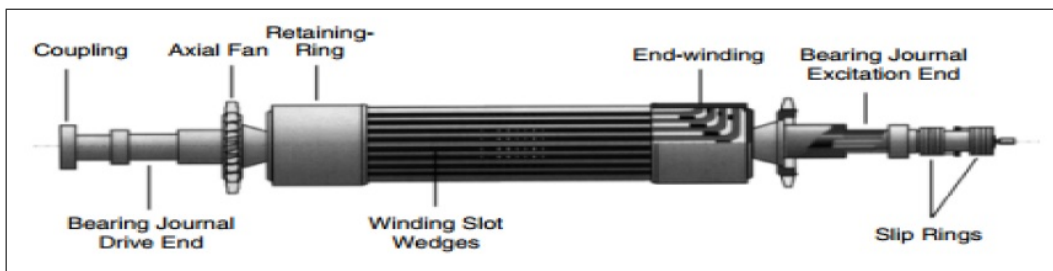
Figure 1.2: Schematic of retaining ring location in a generator rotor. [1]

The retaining rings are under huge stress from a number of sources. The obvious ones are the loading of copper and its own weight. In addition, the rings are under considerable stress at rest because of the shrink-fit. When rotating the underside distribution of the copper loading on the rings is not completely even and the shrink-fit stiffness from pole to winding face is

2

variable—both of which lead to ovalizing effect. Bending stresses come into play from standstill to operation at speed, as the rotors undergo deformation in this range. As a result, retaining-rings are subjected to the high-strain low-cycle effects of start/stops, as well as high-cycle stress modes in operation. The ring material is very critical because of the high stresses. It is mostly non-magnetic in nature with almost the same conductivity as rotor forging. The most common material used is 18% Mn-18%Cr (also called 18Mn-18Cr or simply 18-18). This material has the additional benefit of being highly resistant to aqueous stress corrosion pitting and cracking owing to the high chromium content. Prior to the 18Mn-18Cr rings until the mid–1980s, the most common nonmagnetic material was 18 Mn-4Cr or 18Mn-5Cr, which had the problem of stress corrosion cracking (SCC) when moisture contamination was present.

1.2 EPRI Survey of the Performance of 18-18 Retaining Rings

The industry survey [2] by EPRI assessed operational history of the 18-18 alloy to find problems with these retaining rings. It identified three event-driven damage mechanisms for 18-18 rings: arcing, fretting and corrosion. The most prevalent mechanism found was arcing damage between the ring and either the rotor or the amortisseur winding. Nearly half of the 10% of the total ring population that had some form of damage was attributed to arcing. Of the approximately 3% of the total population of rings represented in the survey that could not be repaired and were subsequently replaced, nearly three quarters were retired because of arcing damage. The major regions of arcing damage were identified as the retaining ring shrink seat, rotor teeth at shrink seat, rotor wedge slots and short slot wedges to rotor steel. Additionally, many of the arc-damaged rings came from Australia and New Zealand. Arcing occurred in Australia and New Zealand 10 times more often than in the rest of the world. Figure 1.3 shows an image of arcing marks in the retaining ring and Figure 1.4 shows arcing in the rotor teeth.

Figure 1.3: Arcing marks on retaining rings [3].

Figure 1.4: Arcing marks on rotor teeth [3].

1.3 Research Methodology

We begin by performing mock-up experiments to extract the contact resistance between an iron piece and 18-18 retaining ring at different contact pressures and different surface conditions. The resistance values thus obtained will indicate if they are high enough to produce the required voltage for the breakdown of the medium. Further, 3-D transient FEA simulations are performed simulating a sudden opening of a small contact area in the shrink fit region to see if the voltage generated meets the arcing criteria.

1.4 Impact of Research

Thermal power plants produce the majority of power in the world today and will continue to do so in the near future. While new thermal power plants are not as likely to be installed, the old power plants need to be more robust and reliable than before. The retaining ring is the most highly stressed component of the whole turbogenerator and even a small defect can quickly translate into a big disaster if undetected. This research will help the machine designers find ways to reduce the arcing and the power plant operators make important decisions relating to generator operation. The remainder of this thesis is organized as follows. In Chapter 2 a brief background is provided about the structure of the rotor and types and origin of secondary currents in rotor. A short note is provided about the prerequisites for arcing and the difference between arcing and sparking. Chapter 3 presents the literature review which includes a review of surveys on arcing in retaining rings and effects of negative sequence currents on rotors. Chapter 4 details the experimental methods used in this study. Chapter 5 discusses the results obtained from the experiments and simulations. Chapter 6 discusses the possible future work and finally Chapter 7 concludes the thesis.

CHAPTER 2

THEORY

2.1 Anatomy of the Turbogenerator Rotor

It is important to know about the generator rotor which consists of many parts in addition to retaining rings. They will be discussed briefly here.

2.1.1 Rotor Forging

The rotor forging is usually a single-piece solid steel forging made of a highly permeable material as it carries the rotor flux. Very high stresses occur in the rotor slot tooth-roots, shrink-fit area, and in general where there are machined radii [1]. It is subjected to high-strain, low-cycle stresses during start-up and shutdown, torsional stresses in operation and during faults, and high-cycle fatigue due to rotation and self-weight bending. Many surface heating effects come into play from AC fluxes arising from cross-slot leakage flux, negative-sequence operation, motoring and slip, etc. Shaft torsional oscillations resulting from power system sub-synchronous resonance, sudden short circuits, and load rejections can cause transient torques in the rotor and significantly affect forging life. These can stimulate torsional natural frequencies and cause the rotor to go unstable. Figure 2.1 shows a 2-pole rotor forging.

2.1.2 Rotor Winding Slot Wedges

The wedges hold the copper winding and its insulation systems in place at high rotational speeds. The wedges are generally made of lightweight materials, such as aluminum or brass, in the winding slots. Since this area does not generally carry the useful magnetic flux, the wedges do not need to
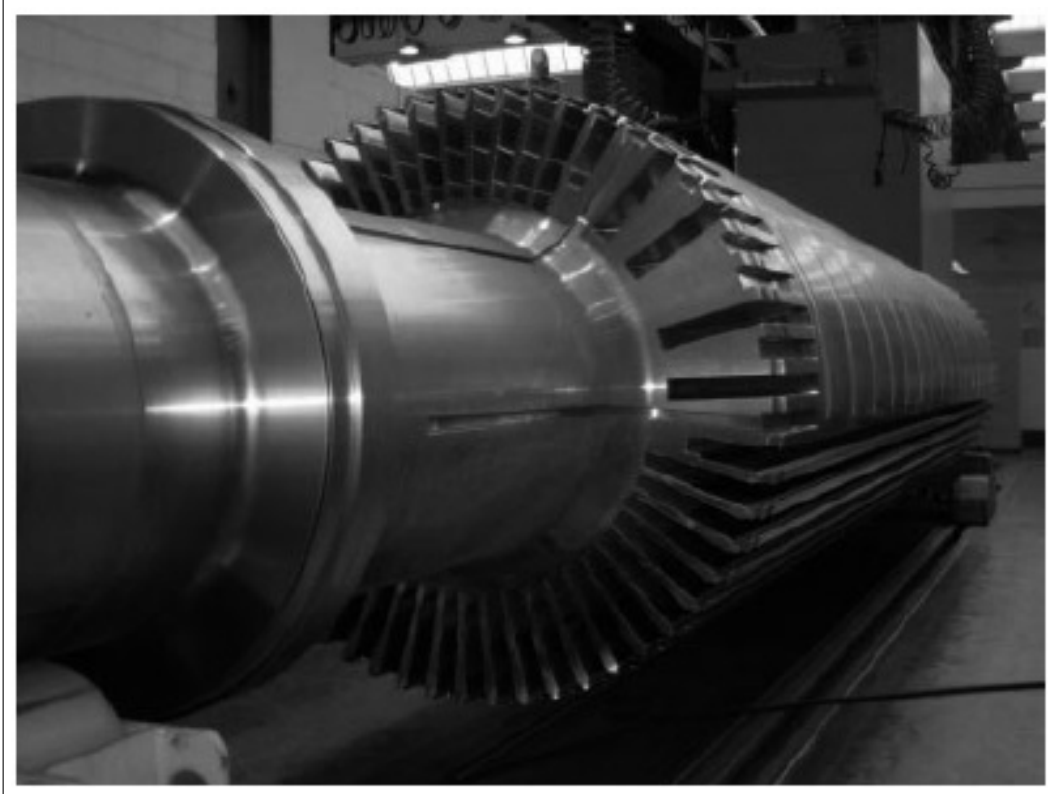
Figure 2.1: Rotor forging for a 2 pole machine [1].

.

be made of magnetic material. The wedges do not sit tightly in the slots and have a relatively loose fit to allow the copper winding underneath to expand axially during operation [1]. Expansion of the copper winding under load can create an enormous axial shear force in the winding slots. Figures 2.2 and 2.3 show images of rotor slot wedges with cooling vents machined on them.

2.1.3 Amortisseur Windings

The amortisseur winding, also known as damper winding, is a separate winding installed under the rotor wedges and retaining-rings that is connected similar to the squirrel-cage of an induction motor. This is typically in the form of a copper (one designer uses aluminum) sheet(s) that forms a ring to conduct the secondary currents into the retaining ring, by passing the slot wedge ends and shrink seats. It produces an opposing torque when currents flow in it, thus dampening torsional oscillations and increasing the stability of the rotor during system stress events. Additionally, it diverts

Figure 2.2: Short rotor wedge [1].
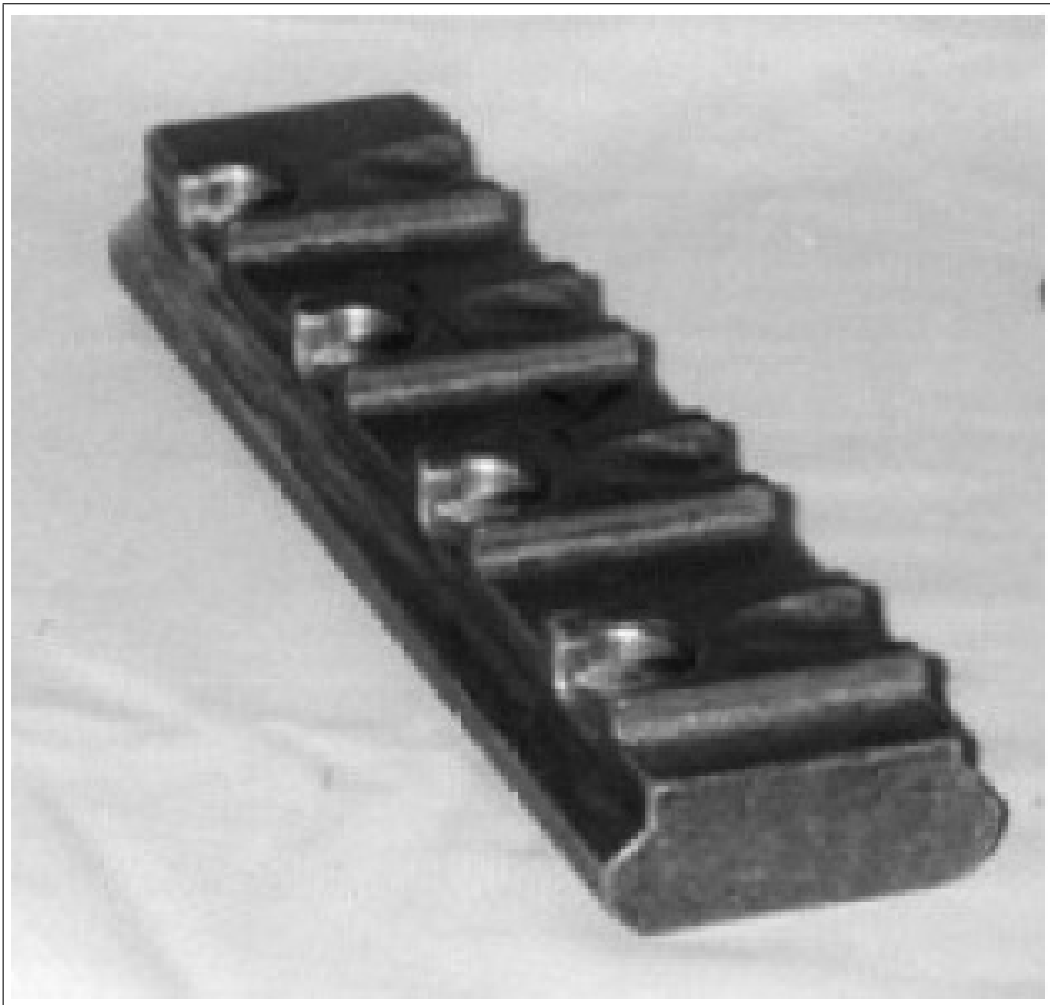
Figure 2.3: Airgap pickup rotor wedge [1].

negative-sequence and motoring currents from flowing in the rotor forging and causing overheating damage. The negative-sequence rating or current-carrying ability of any rotor design is largely dependent on the arrangement and effectiveness of the amortisseur winding. Figure 2.4 shows an image of the amortisseur winding. The larger area of the amortisseur compared to say the slot wedge ends, is aimed at decreasing the current density per area flowing into the retaining ring.
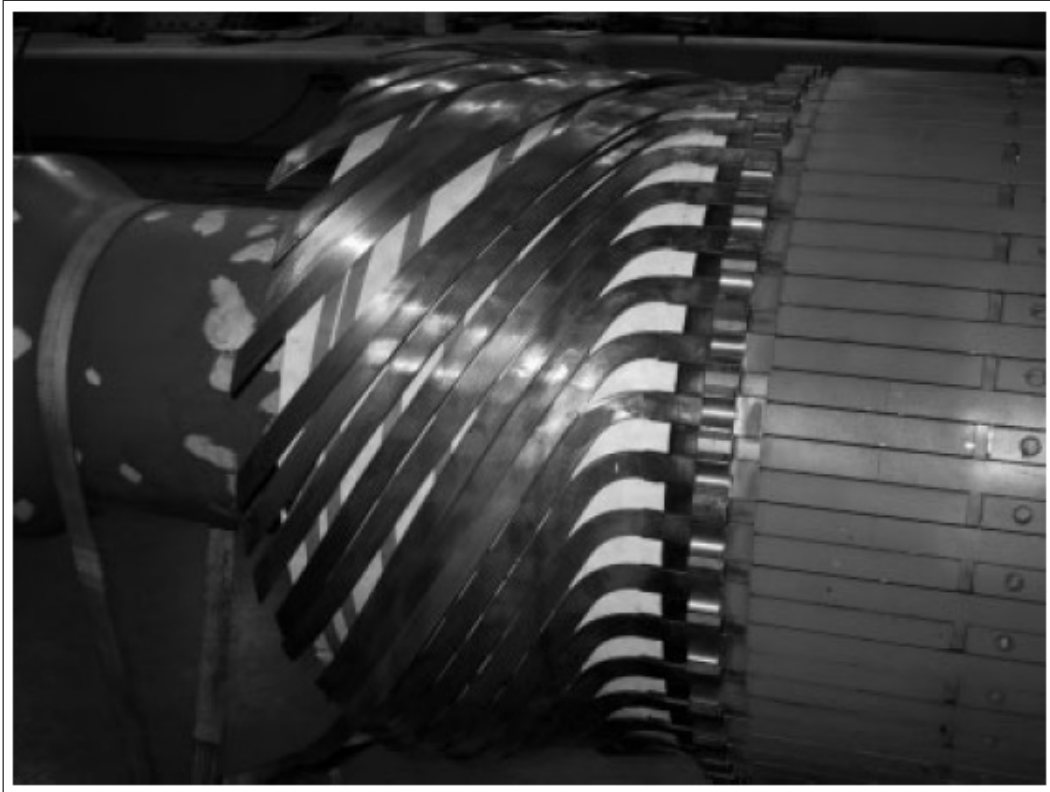
Figure 2.4: Amortisseur winding [1].

2.2   Secondary Currents on the Rotor

Secondary currents of different frequencies can flow on the rotor surface due to a number of events. Some of these events are discussed in the following subsections.

2.2.1 Unexcited Operation ("Loss of Field" Condition)

Operation without field current is potentially dangerous and can occur under a number of circumstances. The following are the two most common circumstances:

1. **Loss of field during operation:** If the field current goes to zero while the generator is connected to the system, the machine starts acting as an induction generator. The rotor operates at a speed slightly higher than synchronous speed and slip-frequency currents are developed [1]. These penetrate deep into the rotor body because of low frequency. The resistance is low because of large skin depth at low frequencies and as such losses are low but it can still produce high heating if the condition persists for a long time.

2. **Inadvertent energization:** If a generator is at rest and the main generator three-phase circuit breaker is accidentally closed connecting it to the power system, large currents are induced on the rotor. The rotor then starts rotating as an induction motor. The very high currents induced in the rotor will tend to flow in its surface, in the forging, wedges and retaining rings. As the rotor accelerates, the currents will penetrate deeper and deeper. The maximum damage occurs while the speed is low and the large currents concentrate in a thin cross section around the surface of the rotor (due to the skin effect). The temperatures generated by the large currents, flowing in a relatively small cross section of the rotor, create very large temperature differentials and large mechanical stresses within the rotor. Other areas are the wedges and in the body-mounted retaining rings, the area where the rings touch the forging and the end wedges [1].

2.2.2 Negative Sequence Currents

A three-phase balanced supply generates a constant-magnitude rotating flux in the airgap of the machine, which rotates at synchronous speed. In a synchronous machine under normal operation, the rotor rotates in the same direction and speed as the main (fundamental) flux. When the supply voltage or currents are unbalanced, an additional flux of fundamental frequency appears in the airgap of the machine. However, this flux rotates in the opposite direction from the rotor. This flux is induced in the rotor windings and
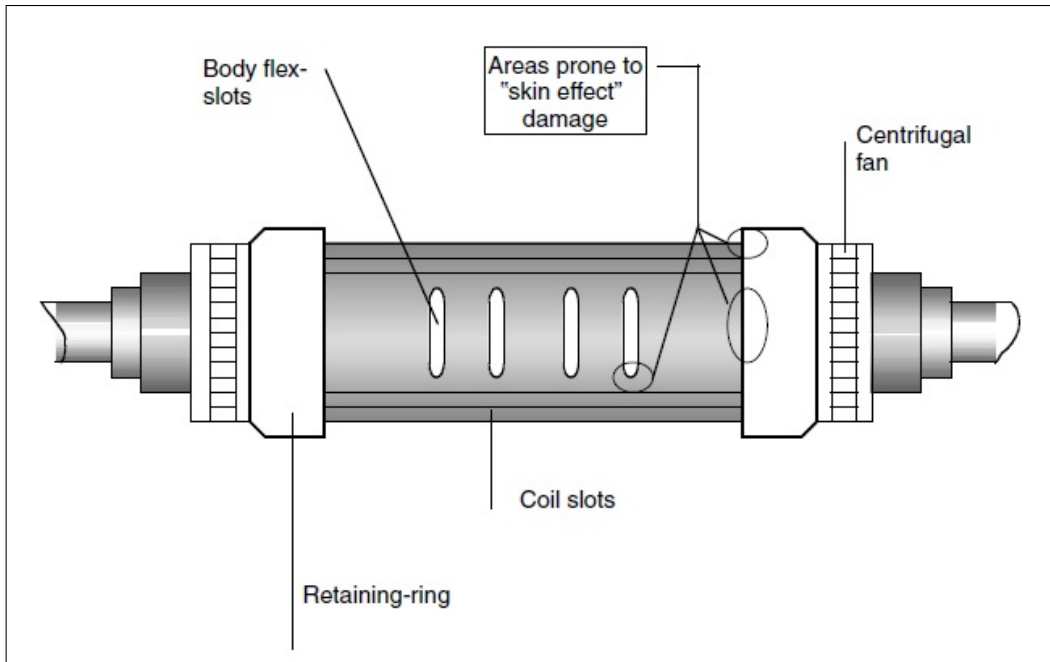
Figure 2.5: Schematic representation of a turbogenerator rotor and the areas most prone to be damaged by the skin-currents generated during inadvertent energization event [1].

body voltages and currents with twice the fundamental frequency. These are called negative-sequence currents. The negative sequence terminology derives from the vector analysis method of symmetrical components. This method allows an unbalanced three-phase system to be represented by positive, negative, and zero sequences. The larger the unbalance, the higher the negative-sequence component. Due to very low skin depth of rotor steel at high frequency, these currents tend to flow on the surface of the rotor. The high effective resistance owing to low skin depth produces tremendous heat leading to damage of end-rings and wedges of round rotors as shown in Figures 2.5 and 2.6.

Negative Sequence currents induced on the rotor surface move from the rotor body out towards the rotor ends [3]. The current path is typically from the rotor body to a slot wedge and then the retaining ring, or from the rotor body to the retaining ring via the rotor tooth (shrink seat). Where there are multiple slot wedges per wedge slot, the current may pass from wedge to rotor back to wedge. Consequently some designs use coatings on the retaining ring shrink area that will enhance conductivity or silver plate the ends of the slot wedges in an attempt to direct any arcing away from the

11
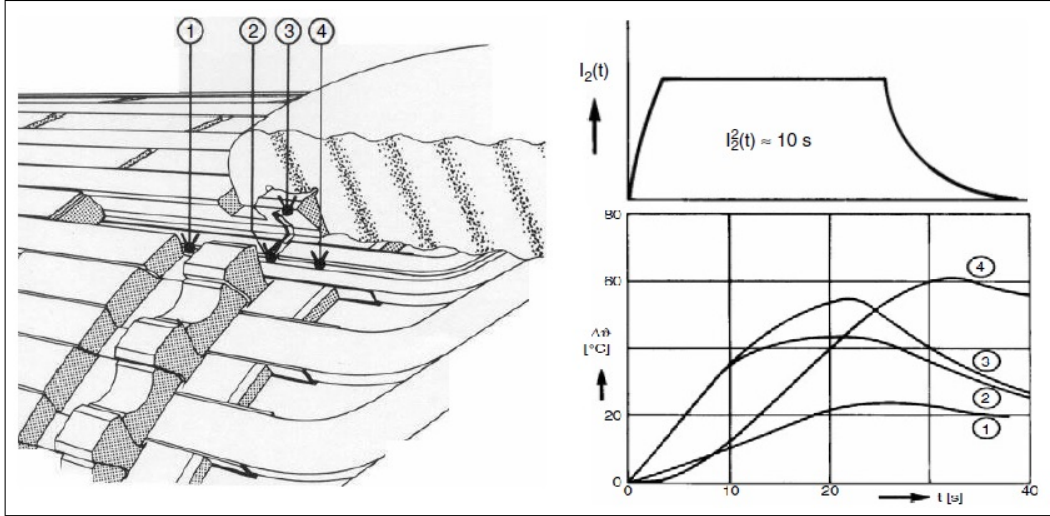
Figure 2.6: Temperature rise measured at the end of the rotor body during short-term unbalanced load operation. (I^2 given in per unit) [1].

highly stressed shrink seat area of the retaining rings.

2.3   Arcing and Its Prerequisites

In 1889, Friedrich Paschen empirically discovered the equation that gives the breakdown voltage—voltage necessary to start a discharge or electric arc—between two electrodes in a gas as a function of product of pressure and gap length [4]. He found that for constant gas pressure as the gap between the electrodes was reduced, the breakdown voltage also decreased but only to a certain point after which it increased at even higher rate. Similarly for a given gap length, reducing the gas pressure showed a similar trend. The curve he found of voltage versus the pressure-gap length product is called Paschen's curve.

The two gas environments commonly seen inside the turbogenerators are hydrogen and air. As can be seen from Figures 2.7 and 2.8, the breakdown voltage required in both the mediums is greater than 300 V.
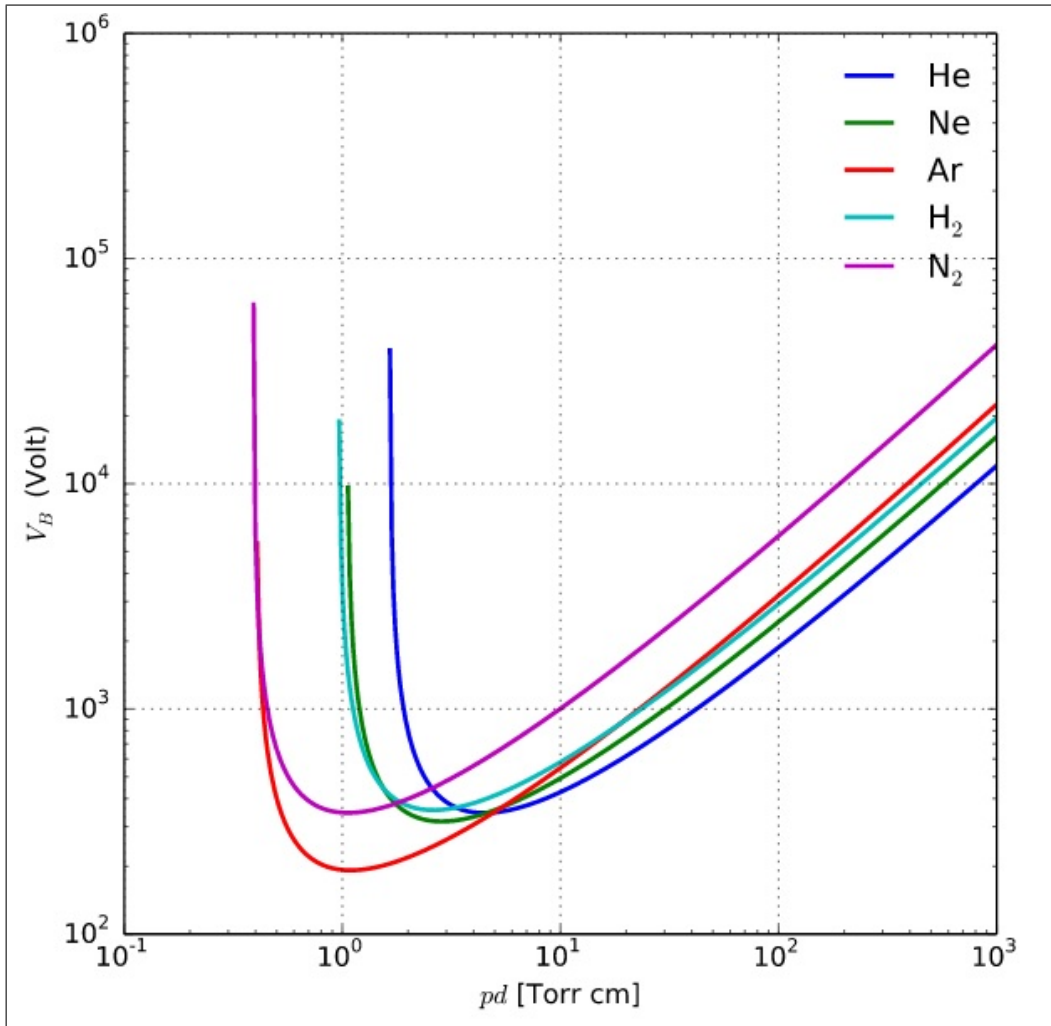
Figure 2.7: Paschen curves obtained for helium, neon, argon, hydrogen and nitrogen using the expression for the breakdown voltage [4].
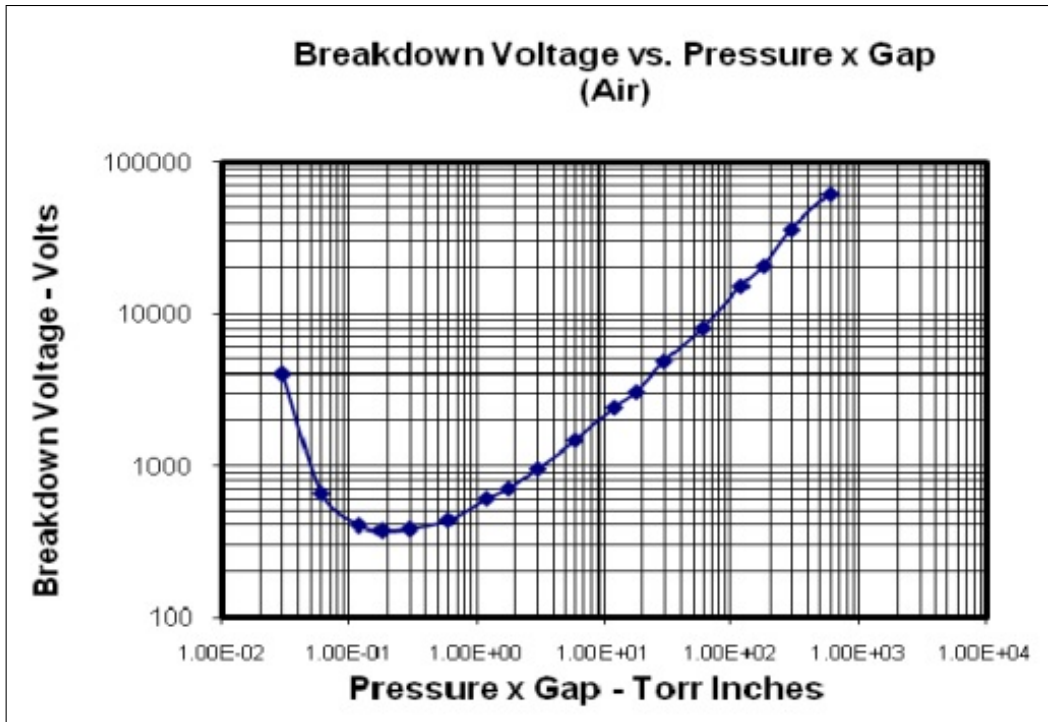
Figure 2.8: Paschen curve for air [5].

2.4 Contact Arcing vs. Sparking

The arc marks found in the retaining rings and other generator rotor auxiliaries can be the result of either contact arcing or sparking or both. As such it is important to differentiate between the two seemingly similar phenomena. Sparking is a high–voltage phenomenon, which occurs when the voltage between the electrodes is high enough to cause the electrical breakdown of the medium. Arcing, on the other hand, can occur at low voltages as well. It occurs when there is a contact break in a current–carrying circuit and the inductance in the system tries to maintain the current flow and arcs in the process. Both the processes follow the Paschen law. These two mechanisms of arcing will be explored in this thesis.

CHAPTER 3

LITERATURE SURVEY

The problem of arcing in retaining rings and other rotor parts is not new and has been discussed in the literature before. In [1], the author cited an incidence of arcing in the contact area between the rotor and retaining ring. It was suggested that the area should be checked for electric pitting or discoloration, indicating current flow. The images of arcing can be seen in Figures 3.1 and 3.2.
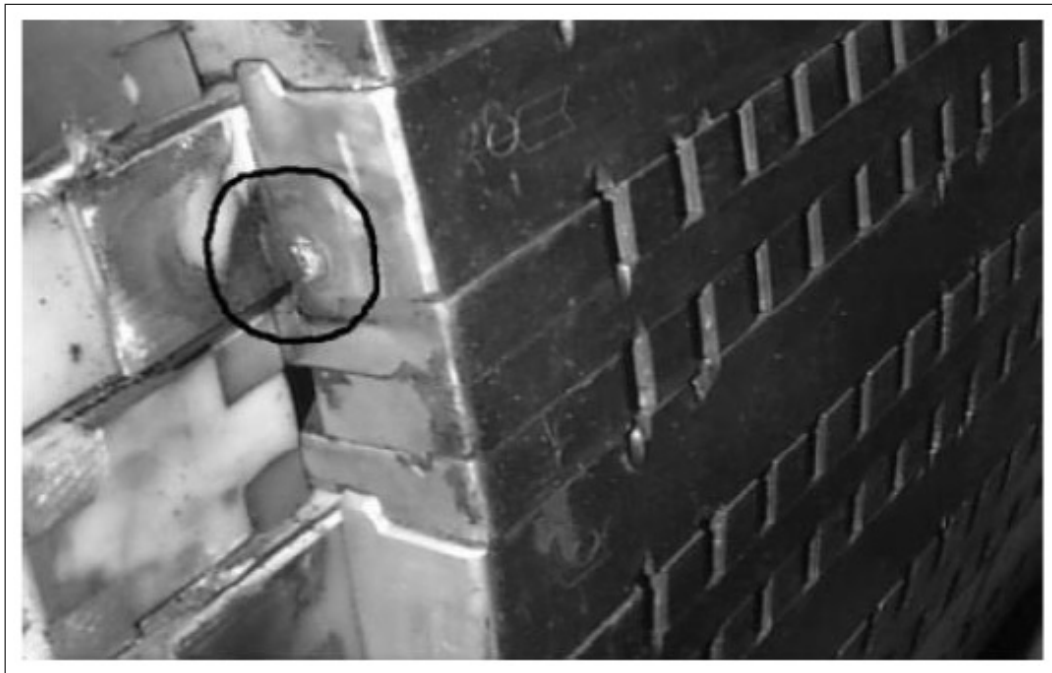
Figure 3.1: The photo shows a "weld" spot formed between the wedge and the retaining ring (not shown–already removed). The "weld" was formed by arcing from surface currents flowing on the surface of the rotor, due to an abnormal operating event [1].

In the survey done by EPRI [2] it was found that arcing was the predominant mechanism of damage in retaining rings. Of the 788 18-18 retaining
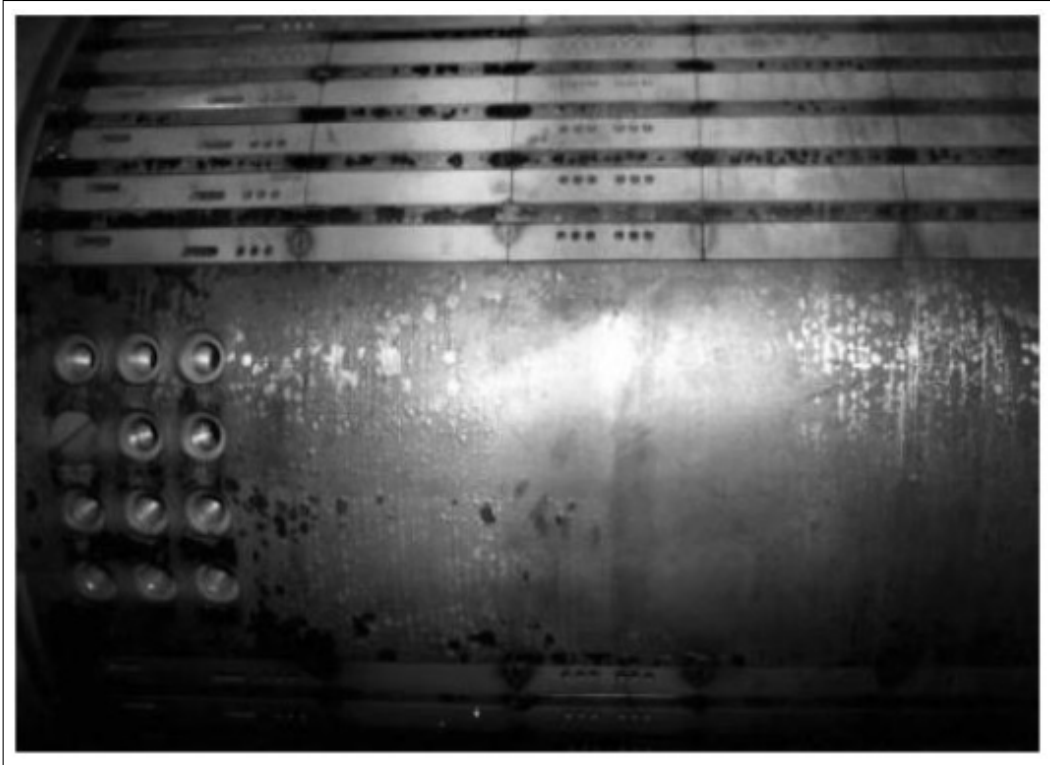
Figure 3.2: Excessive asynchronous motoring developed arcs between wedges and between wedges and tooth, damaging the wedges and the teeth. The excessive heat generated during the abnormal operation also made the paint discolor and flake [1].

rings inspected all over the world, 82 rings had some kind of damage. Of these 82 rings, 39 had arcing problems contributing to 48% of total damage. The detailed survey results are shown in Table 3.1. It can be seen from the table that Australia and New Zealand experienced a much higher damage incident rate than the overall population with a damage rate of 33.3% compared to 10.4% overall. The more revealing statistic, however, is that of 22 rings found to have some sort of damage, 19 had arcing damage due to circulating currents. This represents 28.8% incident rate for arcing damage, a factor of 10x compared to rest of the world.

Based on the peculiar predominance of arcing to a particular geographic location, another survey (see [3]) was done by EPRI in the Australia and New Zealand region. A total of 172 generator rotors were considered in the survey and information was gathered since 1995. A large number of variables were considered to see if they influence extent of arcing damage. The presence of industry that involves large load shifts appeared to have an effect on the

Table 3.1: EPRI Survey Results for 18-18 Retaining Rings [2]

	North America	European Union	Aus/ NZ	Other	Survey Total
Responses (# of Rings)	506	166	66	50	788
Pitting	11	5	2		18
Arcing	14	3	19	3	39
SCC	2	1	1		4
Fretting	5				5
Mechanical	6	4			10
Inherent	2				2
Other	4				4

extent of arcing. Another factor that was deemed responsible for the degree of arc damage was operator training/experience. Arc damage was found all along the current path. It included the rotor wedge slots and rotor teeth at the shrink seat, load bearing surfaces of the slot wedges, wedge ends, and retaining ring shrink seat where arcing occurs either over the location of the end of the slot wedge if arcing was from the slot wedge tongue or at the rotor shrink seat location if arcing was from the rotor tooth. Figures 3.3, 3.4 and 3.5 show some of the images of the arcing from the survey.

Figure 3.3: An example of circumferentially oriented point indications of arc damage on a retaining ring shrink seat as seen during a fluorescent dye inspection and one of the point locations as seen by a low–power digital microscope. As the arcing occurred between two surfaces in close contact, the arcing is level with the adjacent surface of the retaining ring [3].

Retaining ring shrink seat

Rotor teeth shrink seat.

Figure 3.4: An example of extreme arcing where the rotor teeth have been welded to the retaining ring [3].
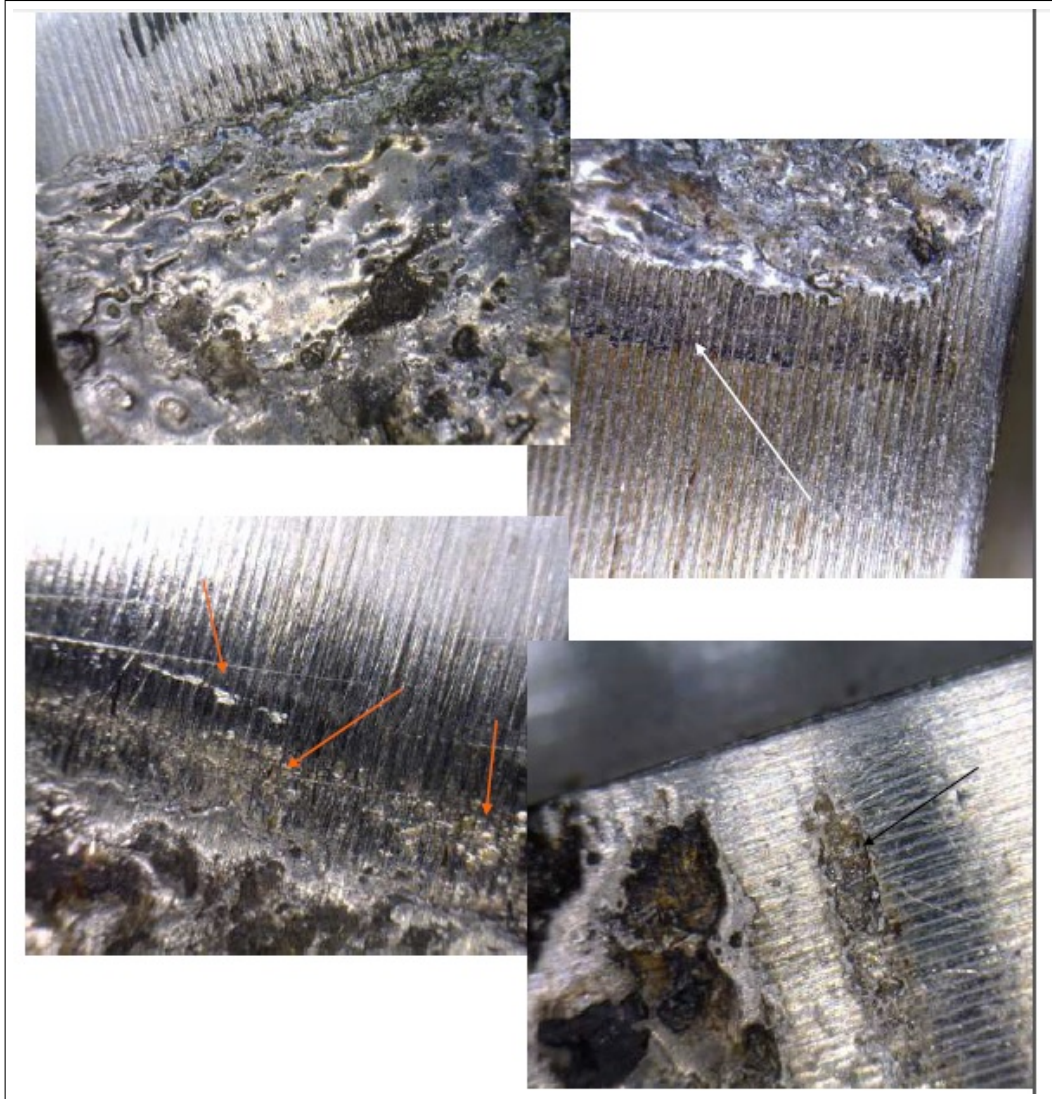
Figure 3.5: A series of images showing different forms of arc damage on a shrink seat, ranging from the large fully molten area (top left), to a heat affected band (top right blue arrow), to aligned pitting of varying degrees of intensity (lower left), to a second linear arc groove adjacent to the main deep damaged area (lower right) [3].

In [6] the authors performed simulations to understand the secondary current flow and distribution in the shrink fit region. They introduced an impedance surface between the rotor and the retaining ring and varied its resistance to see the effect on the current flow. The contact between ring and rotor was assumed to be smooth and continuous, although in reality the contact between two hard surfaces is limited to a few points. Figure 3.6 shows the current path with the ideal contact over the entire region. It

can be seen that current stays very close to the rotor surface due to very small skin depth, taking the shortest possible path into the ring. Instead of spreading out under the shrink fit area, the current crowds into the ring as close as possible to the inboard edge. In Figures 3.7 and 3.8 the impedance surface layer starts slightly away from corner junction. The corner junction still provides a low resistance path and a high current density can be seen there. In Figure 3.9 the impedance effect was seen over the complete surface between ring and rotor. The effect of such geometry is to spread the current across the junction, reducing the current density in the vicinity of the corner. Figures 3.6–3.9 show that as the resistance of the layer increases the current is shifted further from the junction. In the extreme case, where an open circuit develops, the current path would be through the slot material and a sharp discontinuity would exist. In this case, sparking is likely due to the strong field effects.
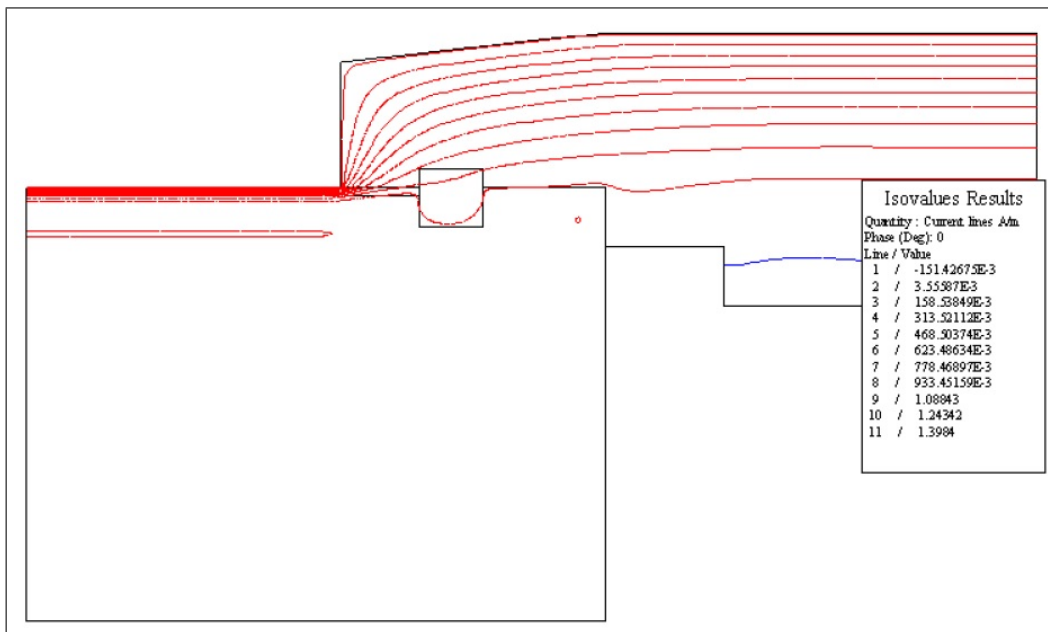
Figure 3.6: Rotor, retaining ring, and slot with ideal surface contacts [6].
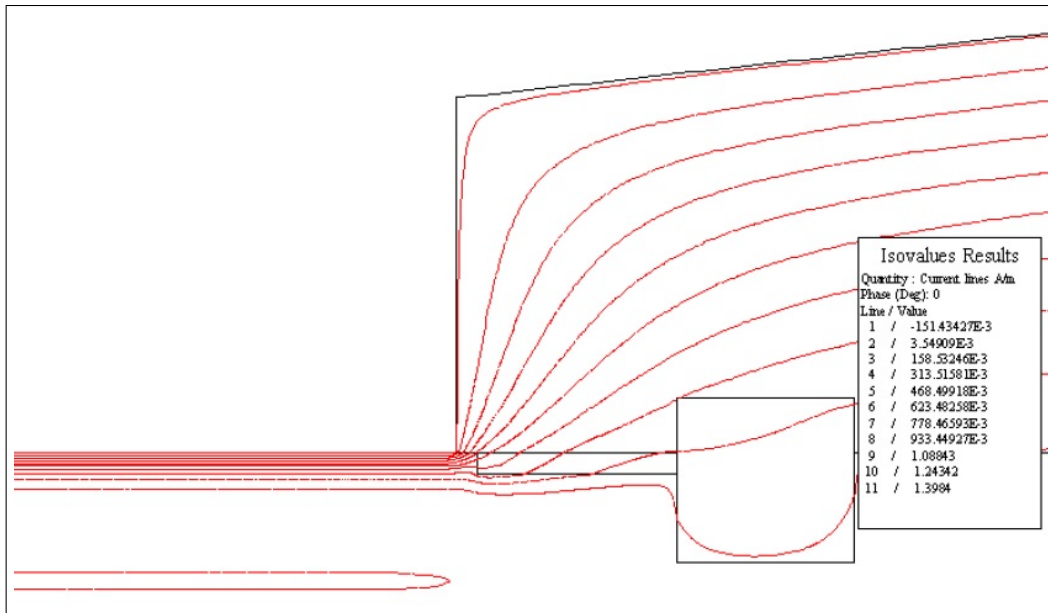
Figure 3.7: Partial impedance surface extending from slot, $\rho = 2.4e^-7/m$ [6].
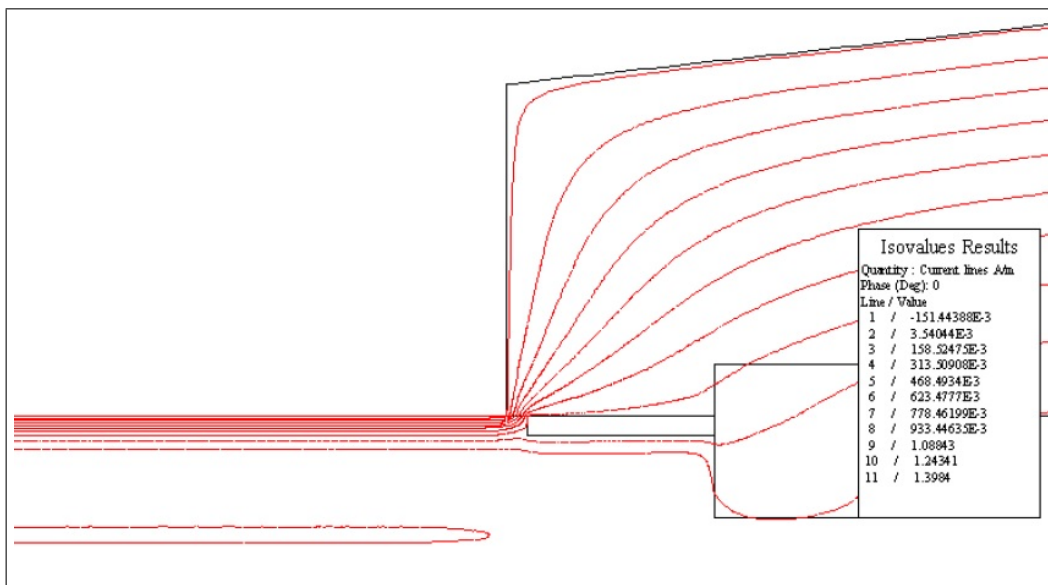
Figure 3.8: Partial impedance surface extending from slot, $\rho = 1e5/m$ [6].
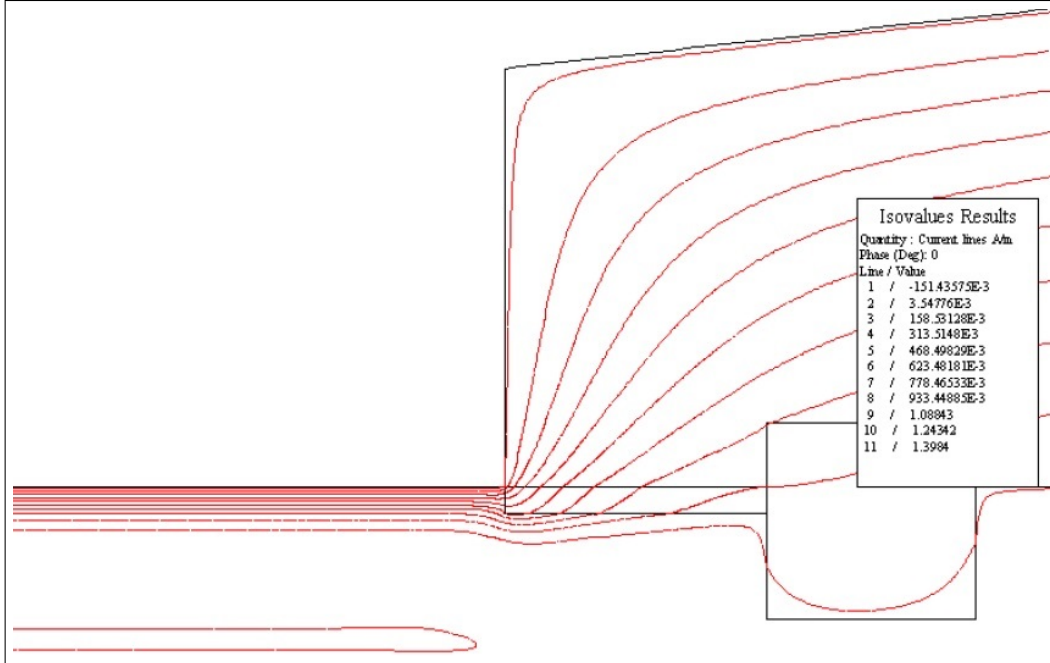
Figure 3.9: Impedance surface from slot to corner, $\rho = 1.0e^-6/m$. [6].

In [7] the authors argued that observed arcing should be due to low values of negative sequence currents, i.e. 100s of amps as compared to 1000s of amps. This is because 1000s of amps would have evaporated material in the order of cubic centimeters per cycle at the fault initiation. Since this has not been observed and most machines have pitting in the range of fractions of a cubic millimeter, it was concluded that erosion occurred during incidents of relatively low negative sequence currents. The authors cited several reasons as to why this might be the case. The faults of very high currents, which result from close-in unbalanced faults, either do not occur or are rapidly tripped by the circuit breaker. The faults resulting in lower currents may persist longer and produce the observed damage.

However, authors of [7] could not figure out how the arc initiates for these low current events. For the high currents, the contact resistance may be high enough to produce a voltage which exceeds the breakdown voltage. For short gaps this is on the order of 300 V from Paschen's curve. For the low current values they suggested two different mechanisms. It is possible that the contact area is very small and a high enough current density exists to create a potential drop large enough to cause a spark. It is also possible that it is arcing and not sparking. During a negative sequence event, the rotor

experiences pulsating torque due to negative sequence currents and significant vibration resulting from this torque. There is also a double frequency radial force on the wedges and the retaining ring shrink fit region. If there is a make-and-break contact at the retaining ring or the wedges, then even a very low current would produce an arc. There is also thermal expansion of the wedges during the negative sequence incident. This may be enough to cause a motion of the wedge as it slips along the tooth. This motion could also be the cause of an arcing event as it touches the retaining ring and recedes.

In [7] the authors analyzed the effects of negative sequence currents on a generator rotor. They explained how stator negative sequence current from a fault can be represented as an equivalent sheet current in air gap. This current was then reflected on rotor body and thermal and mechanical stress analysis was carried out in a finite element software. They introduced a decision–making process for power plant operators so that they can determine if they should go for an inspection of the generator rotor following a negative sequence event. They also discussed the possibility of arcing in the retaining ring.

In [8], the authors presented a multifield and multiscale theory for the interface between two rough surfaces in contact, activated by mechanical load and electric current. At the macroscale a multifield coupling of conduction and induction currents was indicated with heat conduction induced by joule heating. At the mesoscale and microscale, the theory contains a Weierstrass-Mandelbrot description of the rough contact surface profilometry and an asperity-based comprehensive model respectively. Their results indicate dependence of the derived properties such as resistivity on the surface characteristics, external load, and electric current. The electric contact resistance (ECR) at each microcontact between two conductors separated by thin resistive layers consists of several components. First is the constriction resistance due to the convergence and divergence of current flow through the main equivalent conductor and the corresponding constriction resistance of the thin layers, as well as its tunnel resistance due to the presence of an insulating film that introduces a potential barrier that impedes the flow of electrons. The tunnel and the constriction resistances of the thin layer are connected in parallel, while their resultant is connected in series with the constriction resistance of the asperity.

CHAPTER 4

EXPERIMENTAL METHODS

As mentioned in previous chapters, the method of research involved hardware experimentation and software analysis. The hardware experiment was directed towards measuring the contact resistance between an actual sample of 18-18 retaining ring taken from a turbo-generator and an AISI 1018 mild steel, pressed together at very high pressures typical of the shrink-fit region. The mild steel was chosen because an original sample of rotor forging could not be obtained. However, since the electrical and magnetic properties of the two are quite similar, it is believed that the resistance values obtained will be in the same ballpark. These resistance values were then fed to a simulation model which was analyzed in a finite element analysis (FEA) software to measure the steady state and the transient voltage, which develops when a contact opening is simulated. This chapter describes the experiment set-up and the simulation model used in the study.

4.1 Test Plan for the Contact Resistance Experiment

This test plan details the test objectives, configuration, procedure, and data-extraction.

4.1.1 Test Goals

The test aims to achieve following goals:

a. To determine the value of contact resistance between a sample of 18-18 retaining ring and a mild iron under different stress and surface conditions.

b. To obtain any additional parameters such as ambient temperature and humidity for model verification. This model will be used for simulation in software to better understand the phenomenon.
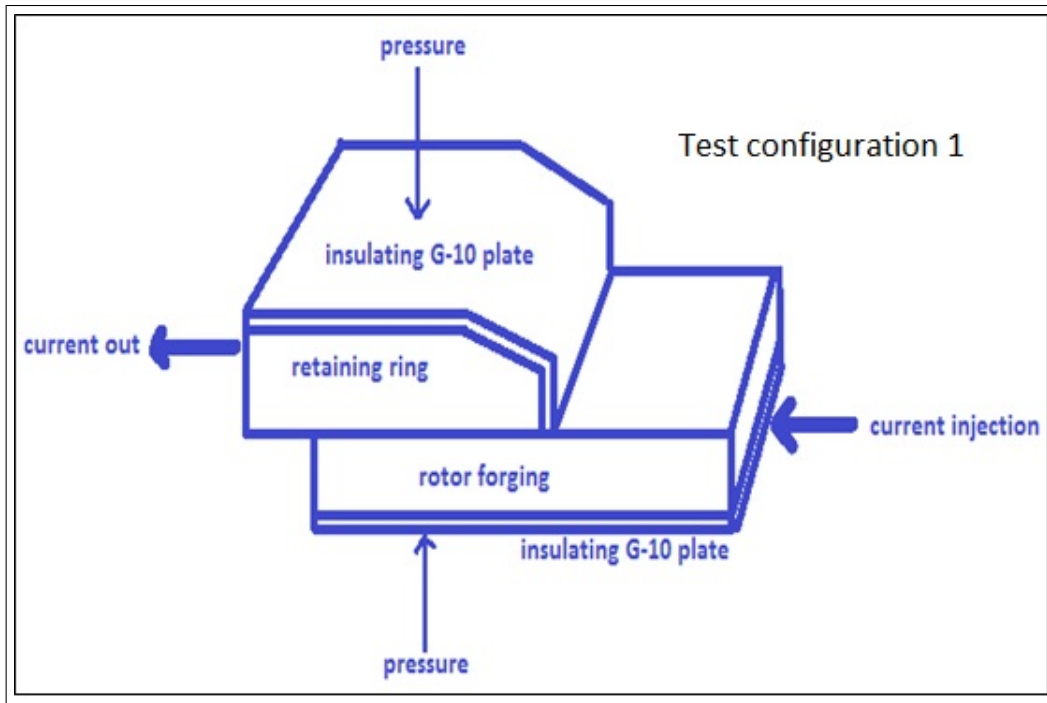
Figure 4.1: Schematic of experimental setup.

4.1.2 Test Configuration

In the configuration shown in Figure 4.1, a retaining ring sample is pressed against a mild steel iron piece at high pressure (up to 20 ksi) and high current (up to 600 A RMS at 120 Hz) is being passed through them. The 120 Hz frequency is twice the nominal operating frequency in the US and signifies the double frequency negative sequence currents flowing in the rotor which are induced from the unbalanced stator currents.

In the actual setup shown in Figure 4.2 a hydraulic compressive test machine is used to apply compressive forces to achieve required pressure values. The current is injected in the retaining ring through a copper crimp that is bolted onto it and is taken out from the iron piece (referred to as steel in the figure) through a similar arrangement as shown in Figure 4.3. Two thermocouples are placed close to the contact region to measure the contact temperature (Figure 4.4). To measure the contact voltage, two wires are taped close to the contact, one on the ring and the other on the iron piece. These wires carry the voltage signals to an oscilloscope. There is a measuring current transformer (Flexcore 7RL-102 1000:5 35VA Current Transformer) which measures and steps down the high current flowing through the samples.

26
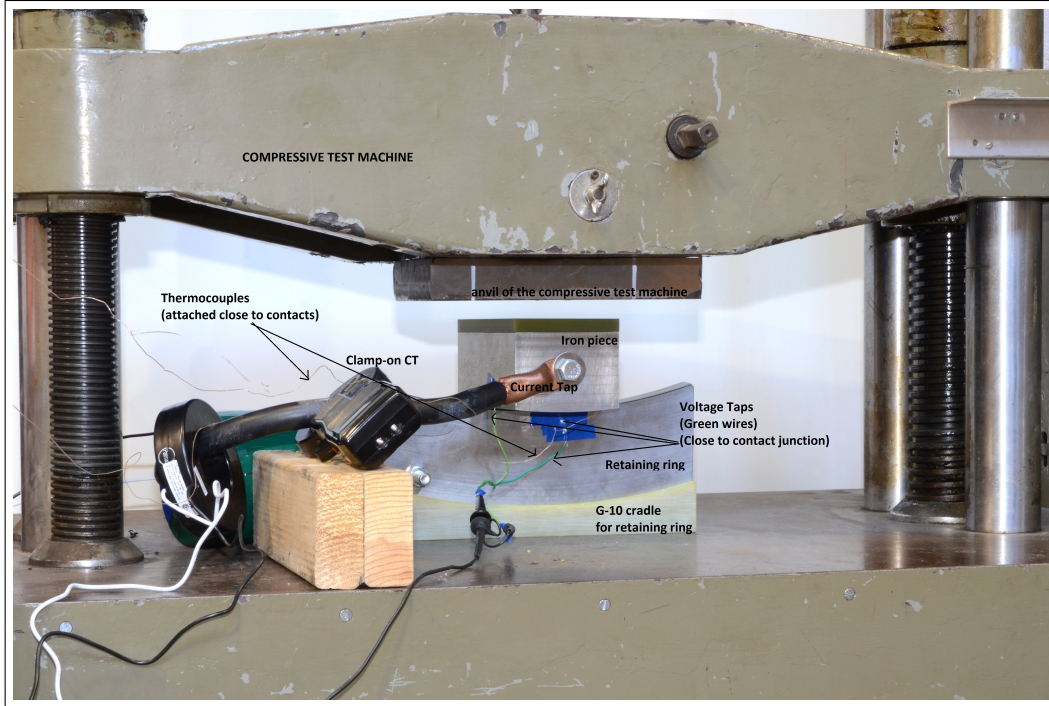
Figure 4.2: Actual test setup showing compressive test machine and the specimens with measuring probes and instruments.

This CT is terminated in a 1 Ω, 100 W power resistor, the voltage across which is also fed to the oscilloscope. Another clamp-on current measuring device (Amprobe) is used to directly measure the amount of current flowing through the samples. Two G-10 plates are used to insulate the anvils of the compressive test machine from the high current. The bottom G-10 plate also acts like a cradle for the retaining ring and provides stability to the overall setup (see Figure 4.5).

G-10 is chosen because of its excellent compressive strength and insulation properties. Figures 4.6 and 4.7 show the setup based on this configuration without the compressive test machine.

4.1.3 Production of High Current

To produce high current ($\sim$600 A) at 120 Hz, a smart power supply (see Figure 4.8) is used with a current transformer. The smart supply used is Pacific Smart Power Supply, and it can provide 2000 kVA, with max 300 V rms and 14 A at any frequency.
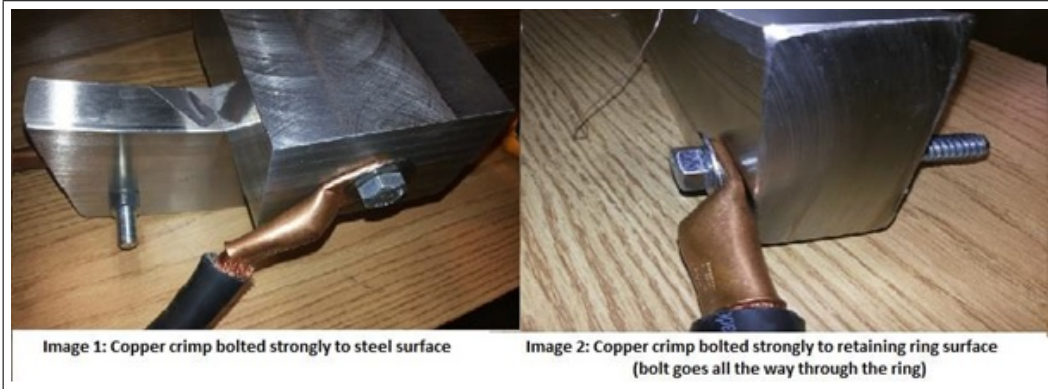
Figure 4.3: Current injection spots in iron piece (steel) and retaining ring.
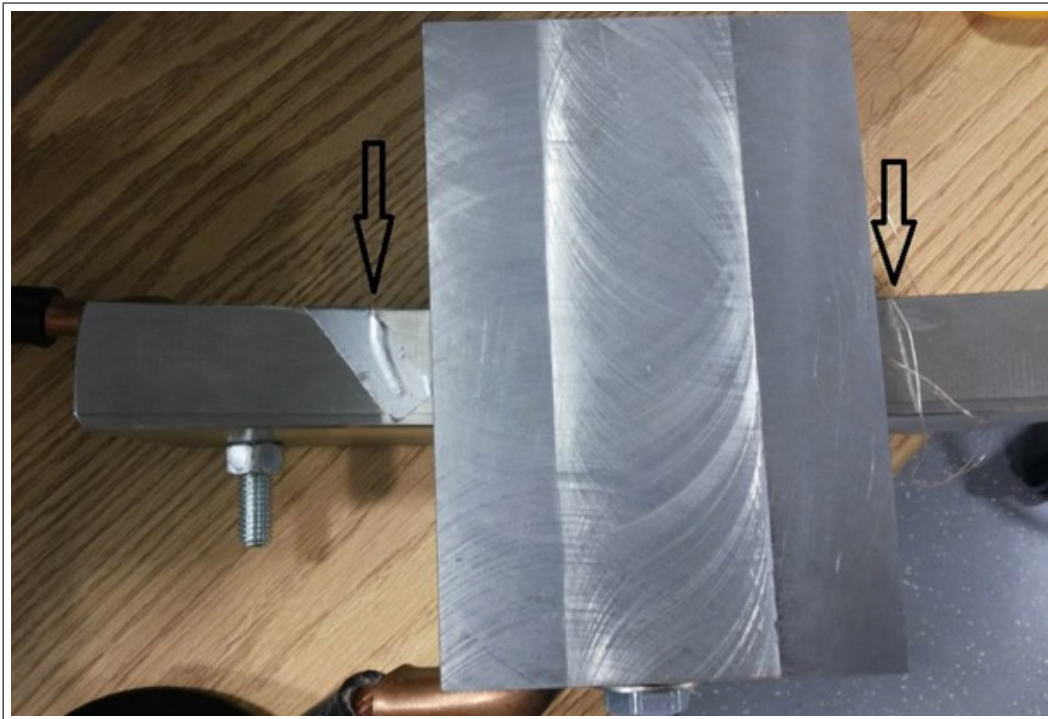
Figure 4.4: Placement of thermocouples close to contact region.

Figure (a) shows the front view of G-10 cradle to support the curved retaining ring from the bottom against the high pressure. This structure provides stability to the whole set-up. The G-10 also electrically insulates the anvils of compressive test machine against high currents. Figure (b) and (c) provide different views of the G-10 cradle.
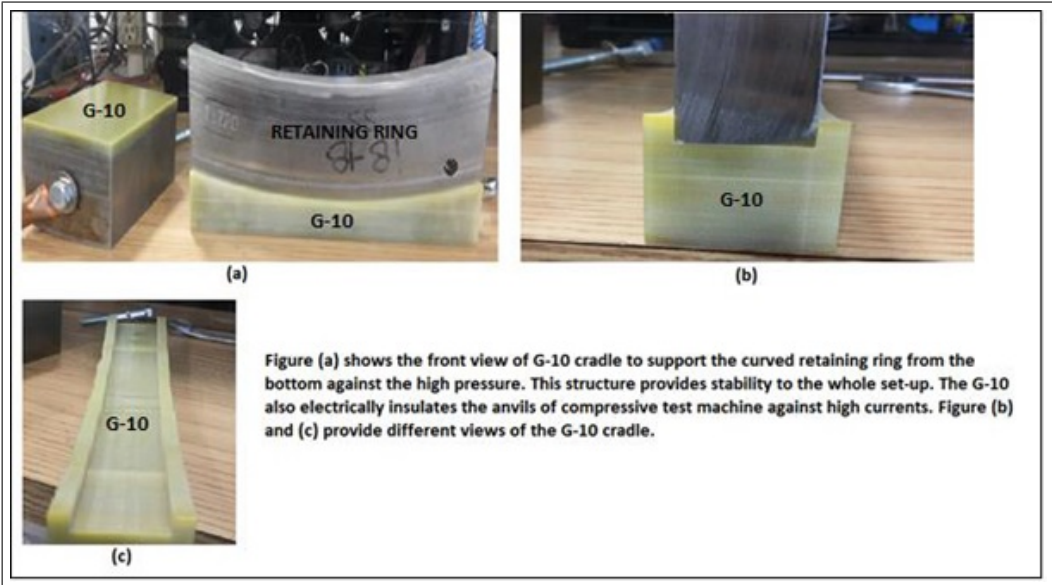
Figure 4.5: The use of G-10 material for insulation and support.

Figure 4.6: Experiment setup without compressive test machine.
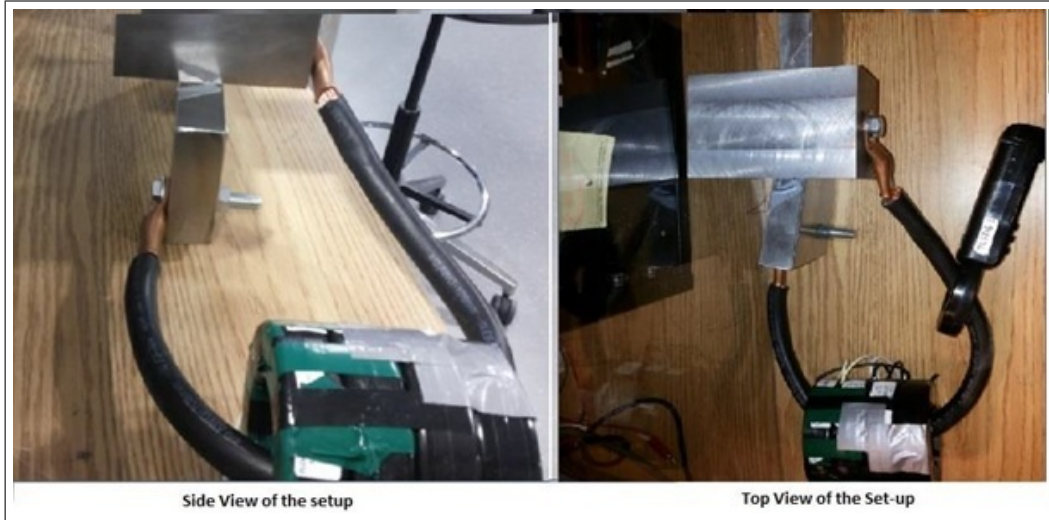
Figure 4.7: Side views of the test set-up.
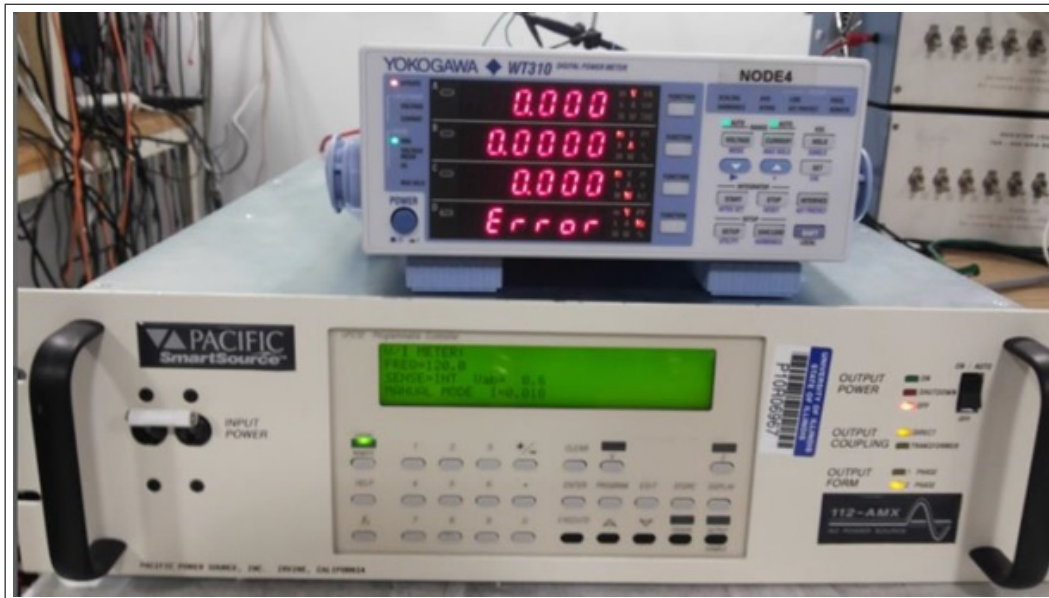
Figure 4.8: Power supply feeding the current transformer in the experiment.

Figure 4.9: Current transformer made by connecting 4 7RL-162 1600:5 45VA CTs in series.

The current transformer consists of 4 Flexcore 45VA 1600:5 current transformers stacked and taped together and connected in series to produce high flux (see Figure 4.9). Four CTs are used to provide sufficient core to the transformer so that it does not saturate.

4.1.4 Measurements

The measurements will be taken in the explained manner. The test will be repeated for 3 different surface conditions. For each surface condition, the test will begin with no external contact pressure (or contact pressure due to just specimens weight) and the pressure will be gradually increased to 20 ksi. The typical nominal contact pressure at the shrink-fit in a generator rotating at rated speed is 10 ksi. For each contact pressure value, the current will be gradually increased from 0 to 600 A at 120 Hz. For each current value, primary voltage, primary current, primary power, voltage between the contacts, secondary current and phase angle between secondary voltage and current will be measured.

4.1.5 Data Extraction

After all the observations have been recorded, meaningful data will be extracted from them. For each value of electric current, contact resistance will be calculated in the following manner:

$$\text{Contact Impedance} = \frac{\text{Contact Voltage}}{\text{Current through contact}}$$

$$\text{Contact Resistance} = \text{Contact Impedance} *$$
$$\text{cosine (angle between voltage and current waveform)}$$

To get the surface roughness value of the iron piece, a small sample (0.5 inches cube) will be taken out from the surface and will be taken to the Materials Research Lab for surface profilometry.

4.2 FEA (Finite Element Analysis) Simulation

In this section the simulation model and the analysis strategy will be described. The software used for the finite element analysis was FLUX 12.1. A 3-D transient analysis was done to better visualize the current density distribution and eddy currents path.

4.2.1 Simulation Model

The simulation model tries to imitate the hardware experiment described in the previous section. As such, it consists of a retaining ring block, a rotor forging block and a contact region in between to model the properties of the contact surface. The model also needs to have around itself an infinite box which permits the user to calculate physical quantities in the air region outside the studied device on different spatial supports. But, as explained later, in this simulation an air region has been used instead, which essentially performs the same function as an infinite box. The model can be seen in Figure 4.10.

These four solid regions are described as volume regions with different magnetic and electrical properties. The contact region is actually made of 9
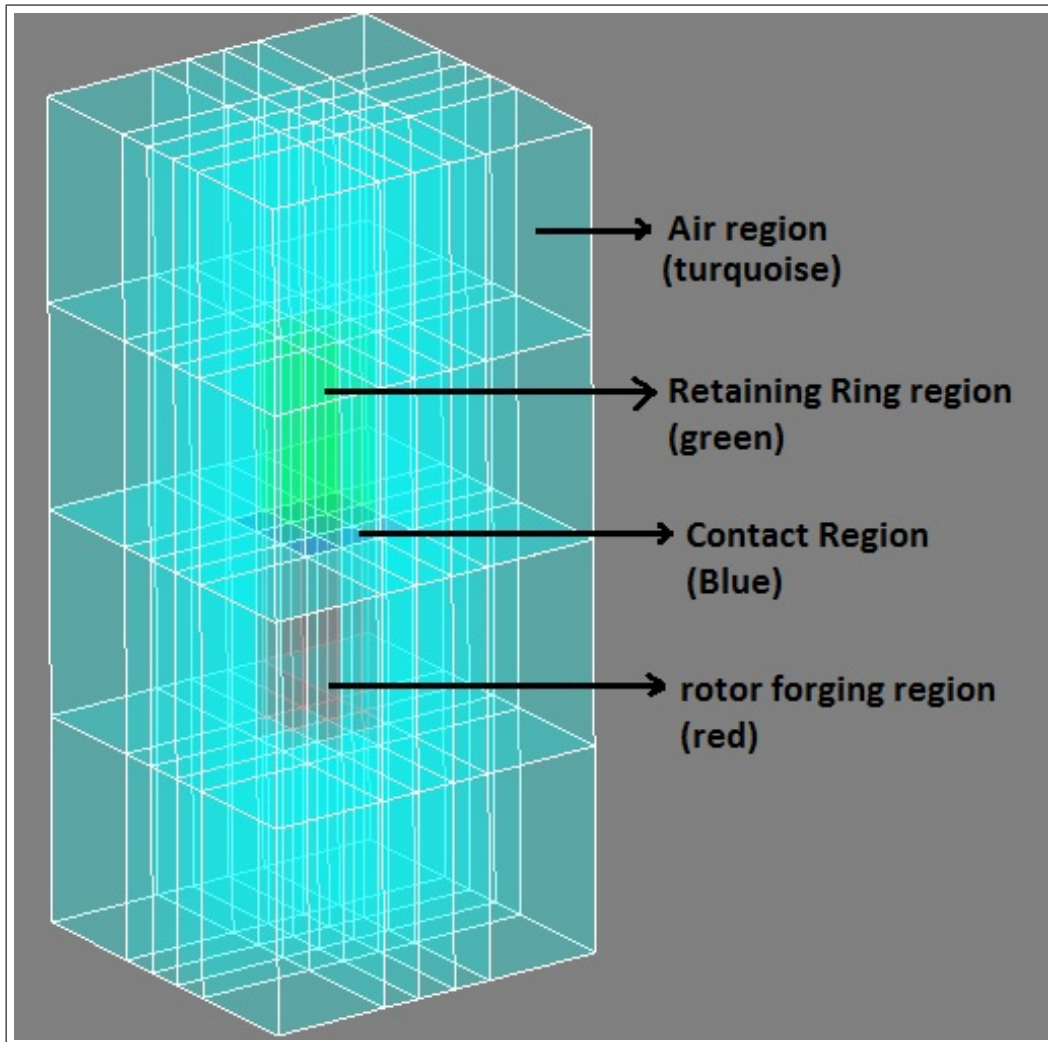
Figure 4.10: Simulation model showing retaining ring, rotor forging, contact and air regions.

Entities	Modify all	CONTACT_MAT...	FORGING	MATERIAL_1	RING
⊟ Ⓔ Material					
Ⓕ Name *		CONTACT_MAT...	FORGING	MATERIAL_1	RING
Ⓕ Comment			linear properties		
⊟ Ⓕ B(H)		☑	☑	☑	☑
⊟ ⓥ Sub types	Initial values	Linear isotropic	Linear isotropic	Linear isotropic	Linear isotropic
⊟ Ⓔ Linear isotropic		Linear isotropic	Linear isotropic	Linear isotropic	Linear isotropic
Ⓕ LIN_ISO *		1500	1500	1500	1
⊟ Ⓕ J(E)		☑	☑	☑	☑
⊟ ⓥ Sub types	Initial values	Isotropic resisti...	Isotropic resisti...	Isotropic resisti...	Isotropic resisti...
⊟ Ⓔ Isotropic resistivity		Isotropic resisti...	Isotropic resisti...	Isotropic resisti...	Isotropic resisti...
Ⓕ LIN_ISO *		4000E-6	0.16E-6	RHO_TIME	0.2E-6
Ⓕ D(E)					
Ⓕ K(T)					
Ⓕ RhoCp(T)					
Ⓕ Mass density (Kg/m³)		false	false	false	false
Ⓕ EIME material					

Figure 4.11: Summary of the material properties of the different materials used.

different symmetrical regions. On a surface level, these can be viewed as 9 different patches of contact. To simulate a localized contact break some of these patches will be opened (electrically their resistivity will be increased to a very high value). These patches of contact, which are opened later, are given a different name. So the contact region consists of 2 different groups of regions: Contact and Contact2. They both have the same electrical properties up to a certain time, after which the resistivity of the Contact2 region is given a step increase. These material properties are summarized in Figure 4.11.

Material1 is the material used for Contact2 region. It uses a time varying resistivity, RHO_TIME whose description can be seen in Figure 4.12.

A mapped meshing was used for meshing the 3-D model. This, in contrast to the aided meshing of the FLUX Software, is simple and leads to fewer elements and hence is less computationally complex. It is user–defined and customized to fit user needs. In addition, an air region was used instead of an infinite box so that the same mapped meshing can be extended to the air region. Coupled to the above model is an electrical circuit (Figure 4.13) which describes how current will flow through the above setup. All the aforementioned 3 regions are described as one solid conductor in the electrical circuit. A current source supplies the current to the solid conductor. The
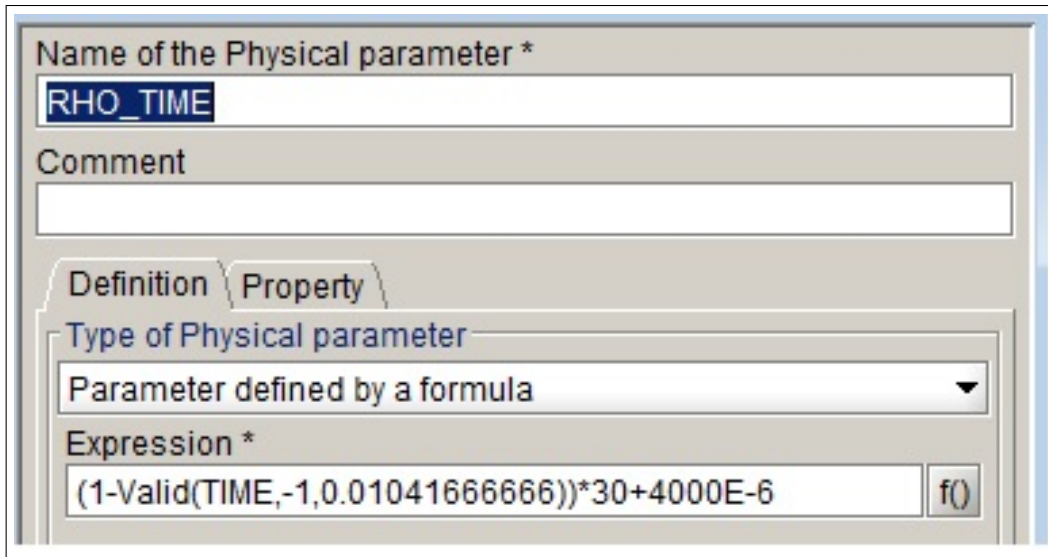
Figure 4.12: Time–dependent variation of resistivity parameter, RHO_TIME.

current value being supplied is

$$I = 1414 * sin(2 * \pi * 120 * t)$$

4.2.2 Method of Analysis

The transient simulation will take place for 3 electrical cycles. For a 120 Hz signal, this corresponds to 0.025 secs. The time–dependent electrical resistivity of contact region Contact2 increases by almost 8 orders of magnitude signifying opening of a small patch of contact. The rest of the contact region Contact, still has small resistivity and carries the bulk of the current after Contact2 opens up. The main parameter of interest is the voltage across the Contact2 region. Getting the voltage drop is not straightforward in FLUX software, so an indirect route was chosen to calculate the voltage. In this indirect method, first the power loss in the volume region Contact2 was calculated and then it was divided by the amount of current flowing through the region. To calculate the amount of current flowing through Contact2, the normal component (i.e. normal to the surface and in the direction of current flow) of the current density vector was integrated over the Contact2 surface. The PyFlux code given in Appendix D shows how this is carried out. The code also generates all the required plots.
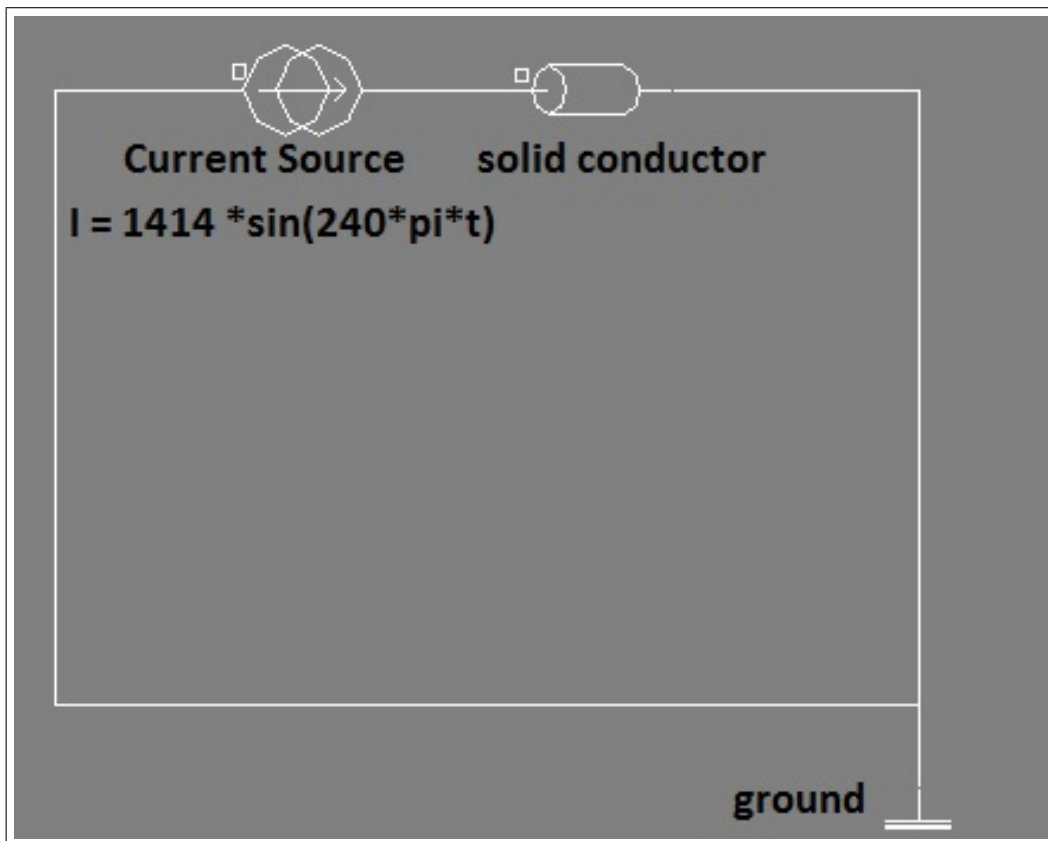
Figure 4.13: Electric circuit coupled to the simulation model. A current source is connected to a 2 terminal solid conductor.

CHAPTER 5

RESULTS AND DISCUSSION

This chapter presents and discusses the results obtained from the hardware and software experiments described in the previous chapter.

5.1 Contact Resistance Experiment Results

This experiment was performed and repeated for 3 different surface conditions of the mild iron piece. First it was made smooth and then sandblasted for a rough texture and finally the rough surface was left to rust. The surface of the retaining ring was kept same throughout the different experiments. After each experiment a small section of the iron piece was cut out and taken to the lab for surface profilometry.

5.1.1 Contact Resistance of Smooth Surface

The external contact pressure between the ring and the iron piece was varied from 0 to 20 ksi in steps of 5 ksi, and for each of those pressure values the current was slowly increased until the transformer saturated. The contact resistance values obtained for different pressure values are plotted in Figure 5.1 and 5.2. The recorded data for this experiment is shown in Appendix A.

A small section was cut out from the iron piece and taken to the Materials Research Lab for surface profilometry in a DEKTAK 3030 Surface Profilometer. This profilometer measures the roughness in a linear profile. The roughness was measured in two orthogonal directions. For each direction, the measurement was done for 3 different lines, all parallel to the chosen direction. The points measured by the DEKTAK were further analyzed in MATLAB's curve fitting tool to get rid of any surface curvature. The surface plots for the smooth iron piece in the 2 directions is shown in Figures 5.3
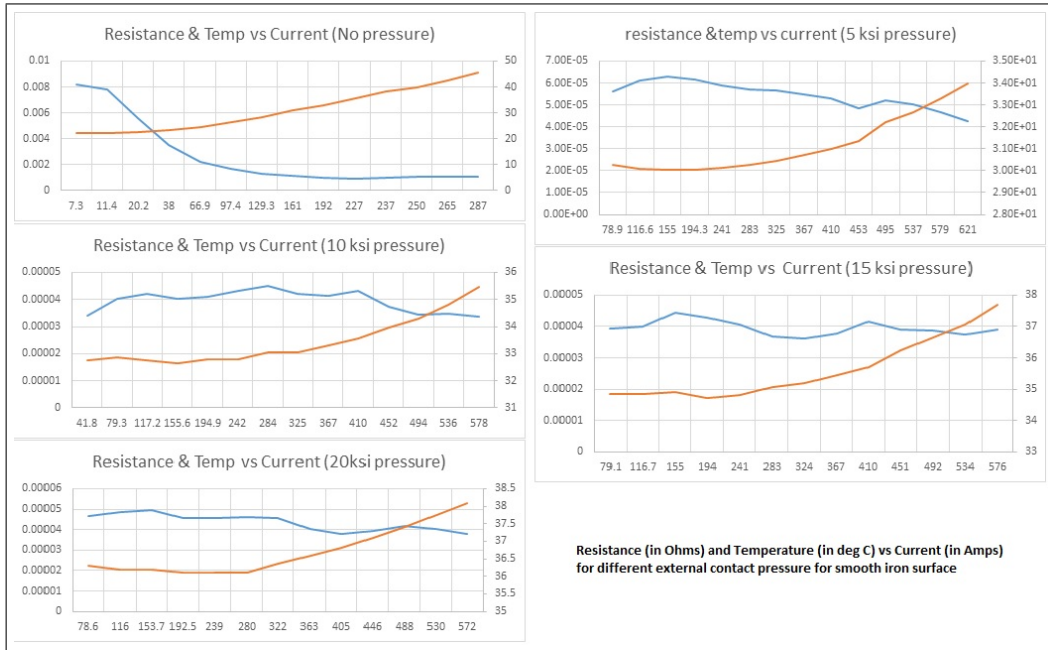
Figure 5.1: Resistance (in ohms) and contact temperature (in deg C) vs. current (in amps) at different contact pressures for smooth iron piece.

Figure 5.2: Resistance (in ohms) vs. current (in amps) at different contact pressures for smooth iron piece.

Figure 5.3: Surface plot of the smooth iron piece in X direction. The bottom plot filters out slight curvature in the top plot.

and 5.4.

The surface plots for the retaining ring in the 2 directions are shown in Figures 5.5 and 5.6.

The rms roughnesses, also known as R_k, obtained for retaining ring and the smooth iron piece are as follows:

R_{RMS}(forging) (in horizontal direction) = 6262.87 Å

R_{RMS}(forging) (in longitudinal direction) = 4020.00 Å

R_{RMS}(ring) (in horizontal direction) = 6378.43 Å

R_{RMS}(ring) (in longitudinal direction) = 43678.00 Å

5.1.2   Contact Resistance of Rough Surface

The smooth iron piece used in the previous experiment was made rough by sandblasting the top surface. The experiment was then performed in the same manner and the same post–processing was done. The contact resistance values obtained for different pressure values are plotted in Figures 5.7 and
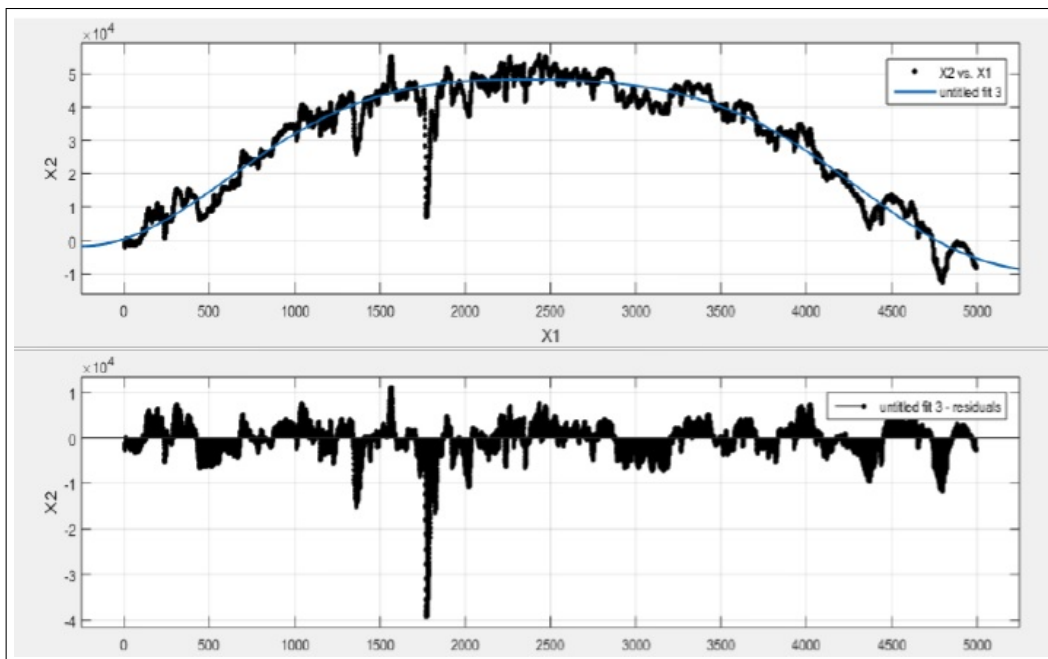
Figure 5.4: Surface plot of the smooth iron piece in Y direction. The bottom plot filters out the convex curvature in the top plot.
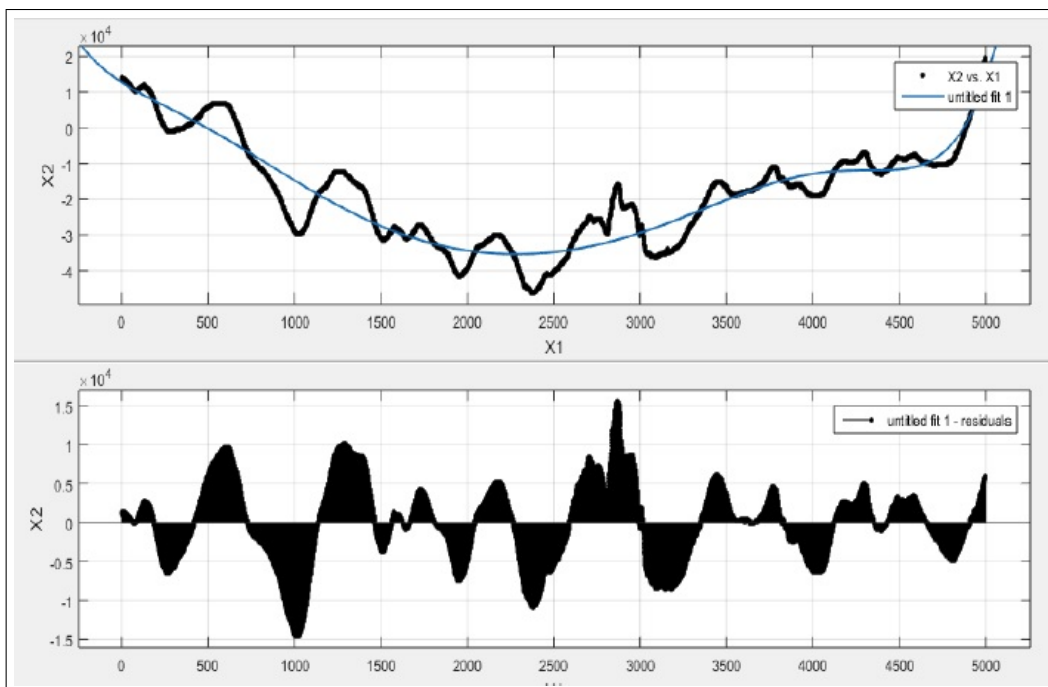
Figure 5.5: Surface plot of the retaining ring in X direction. The bottom plot filters out the curvature in the top plot.
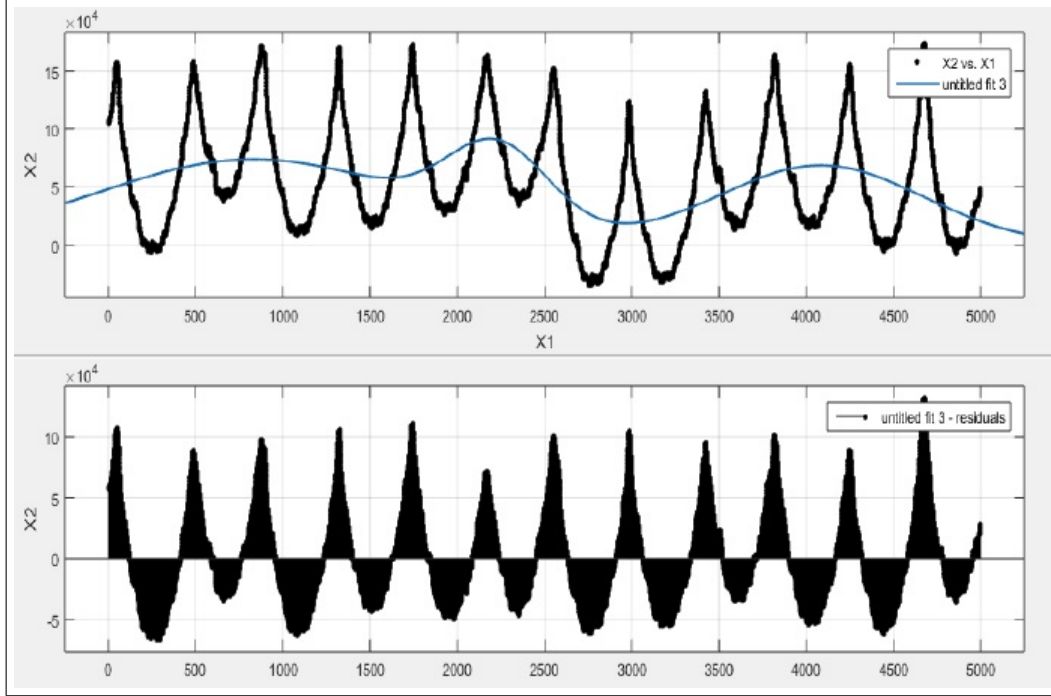
Figure 5.6: Surface plot of the retaining ring in Y direction. The bottom plot filters out the curvature in the top plot.

5.8. The recorded data can be found in Appendix B.

The surface plots in the 2 directions are shown in Figures 5.9 and 5.10.

The rms roughnesses, also known as R_k, obtained for the rough iron piece are as follows:

R_{RMS}(forging) (in horizontal direction) = 18818.67 Å

R_{RMS}(forging) (in longitudinal direction) = 19194.00 Å

5.1.3 Contact Resistance of Rough Rusted Surface

The rough surface of the iron piece in the previous experiment was rusted quickly in about 2 hours by using muriatic acid and copper solution. The experiment was performed in the same manner as before and the same post–processing was done. The contact resistance values obtained for different pressure values are plotted in Figures 5.11 and 5.12. The recorded data for this experiment is shown in Appendix C.

The surface plots in the 2 directions are shown in Figures 5.13 and 5.14.

The rms roughnesses, also known as R_k, obtained for the rough iron piece are as follows:
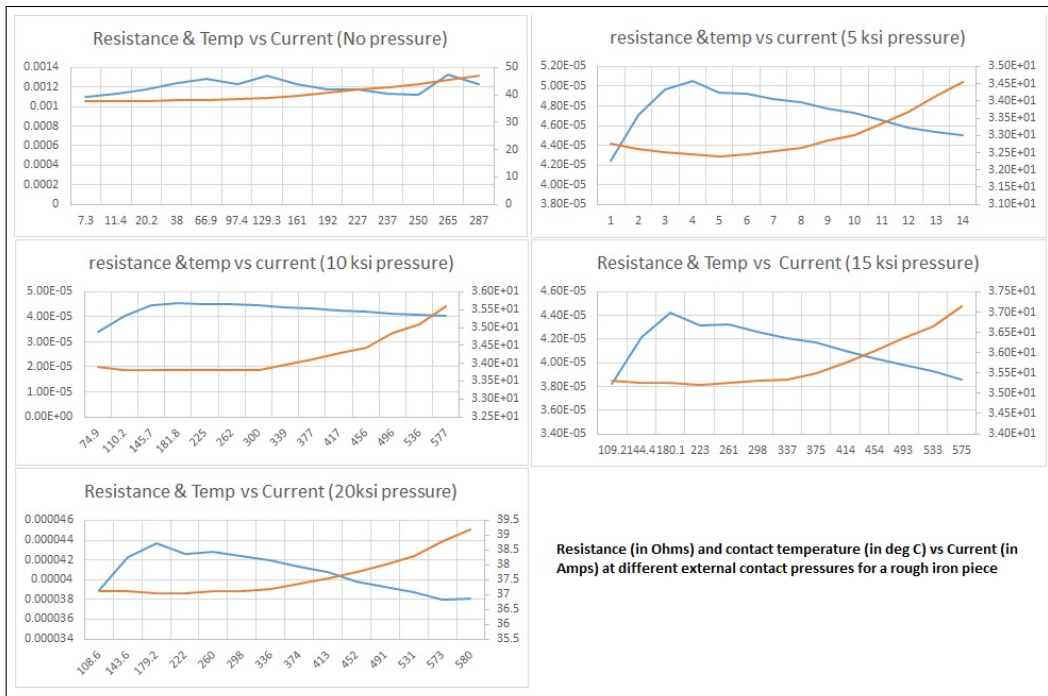
Figure 5.7: Resistance (in ohms) and contact temperature (in deg C) vs. Current (in amps) at different contact pressures for rough iron piece.
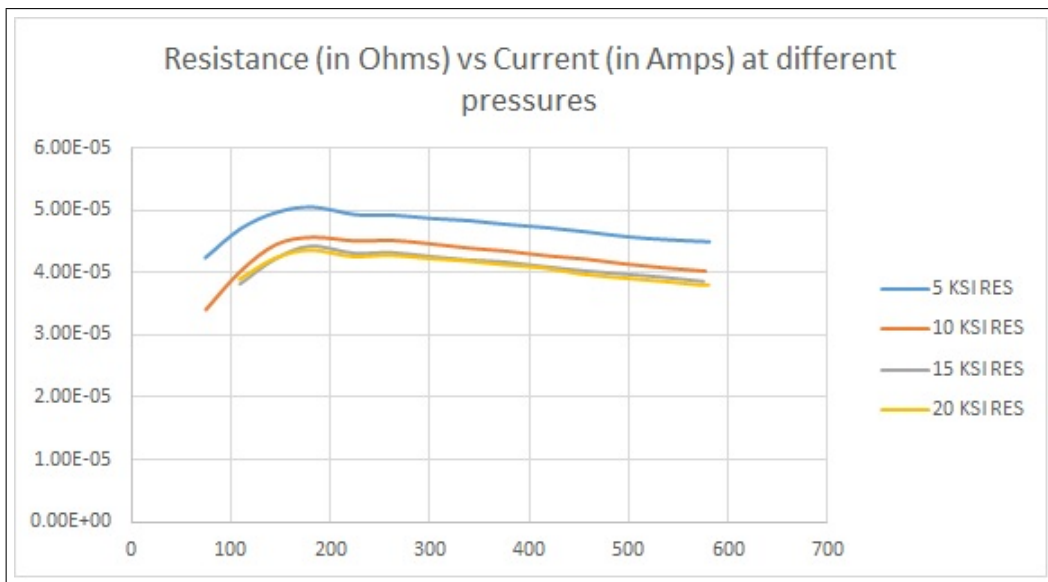
Figure 5.8: Resistance (in ohms) vs. Current (in amps) at different contact pressures for rough iron piece.
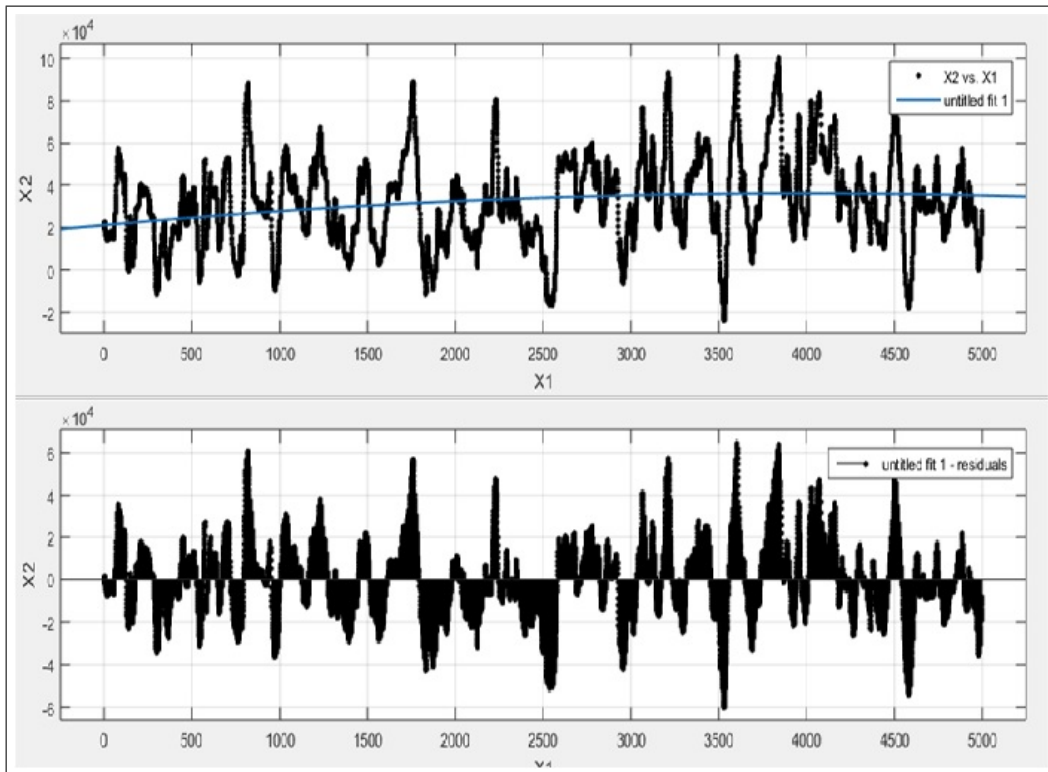
Figure 5.9: Surface plot of the rough iron piece in X direction. The bottom plot filters out slight curvature in the top plot.
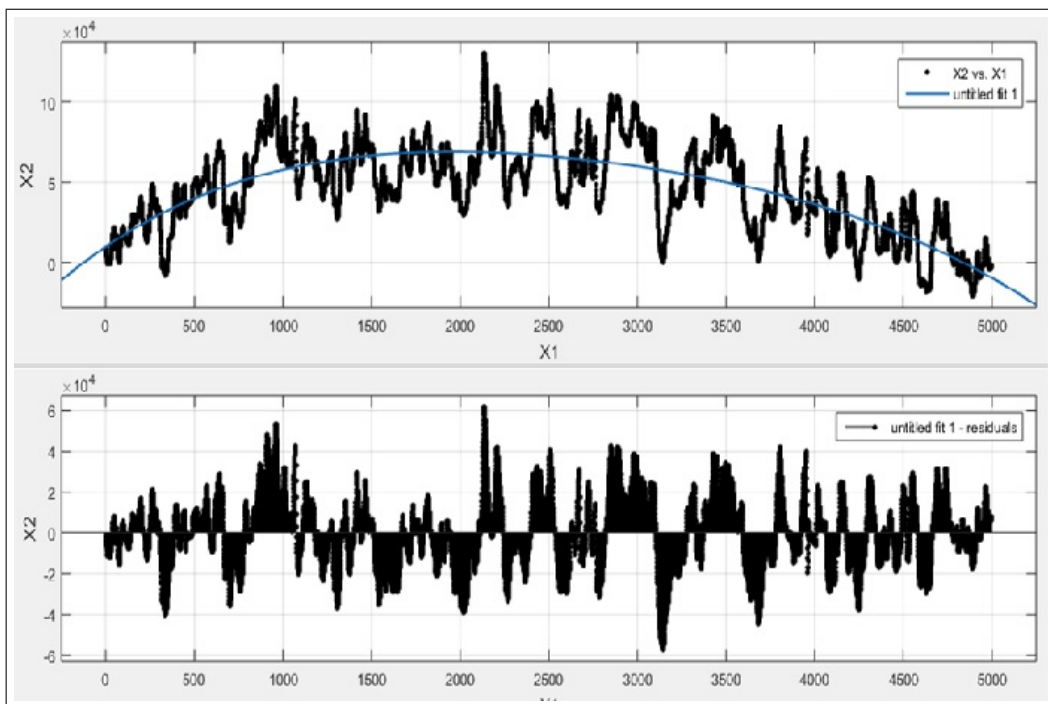
Figure 5.10: Surface plot of the rough iron piece in Y direction. The bottom plot filters out convex curvature in the top plot.
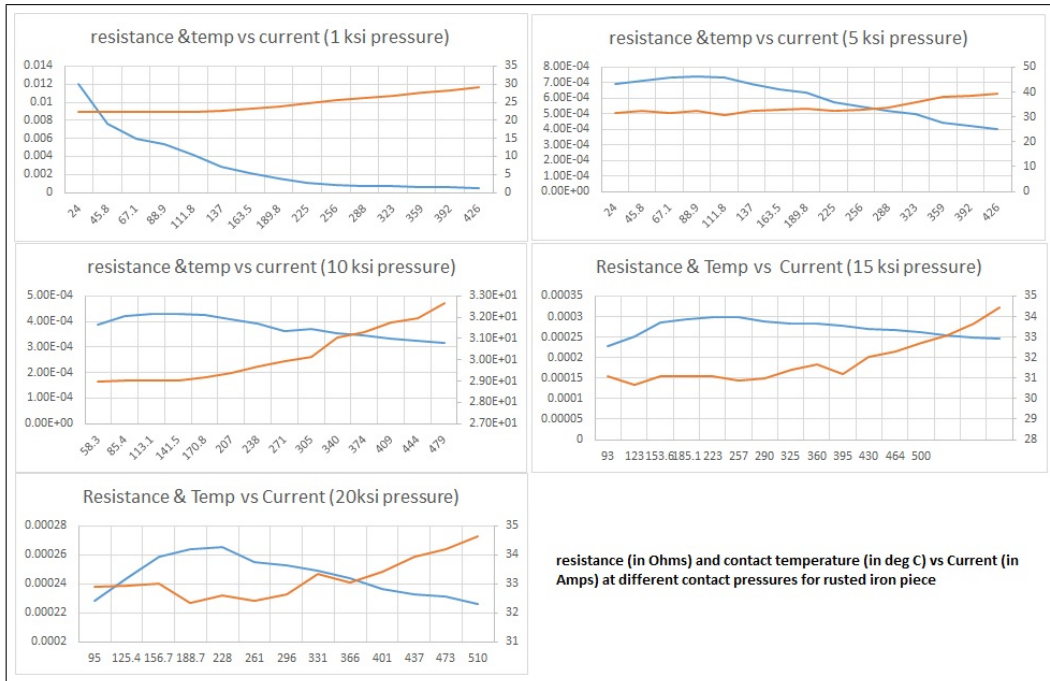
Figure 5.11: Resistance (in ohms) and contact temperature (in deg C) vs. current (in amps) at different contact pressures for rough rusted iron piece.
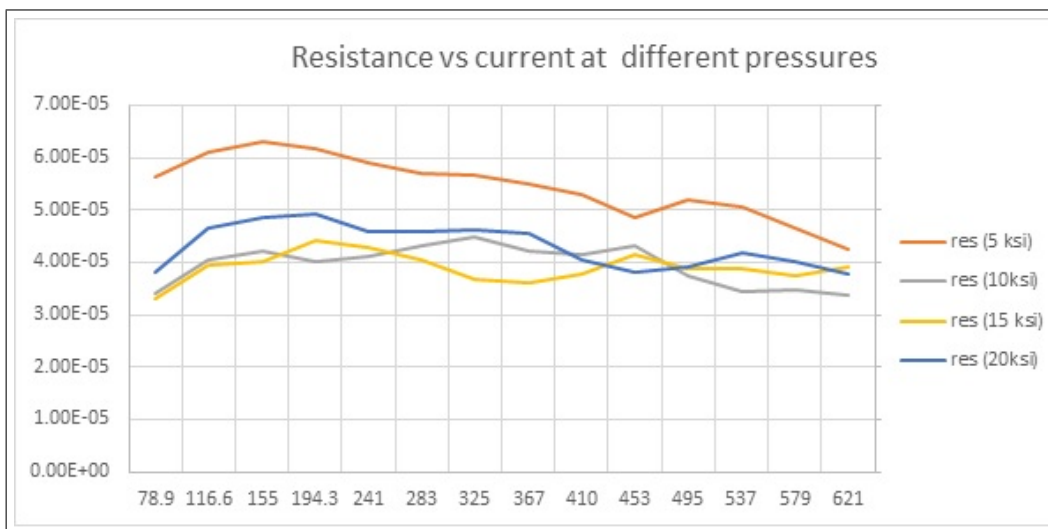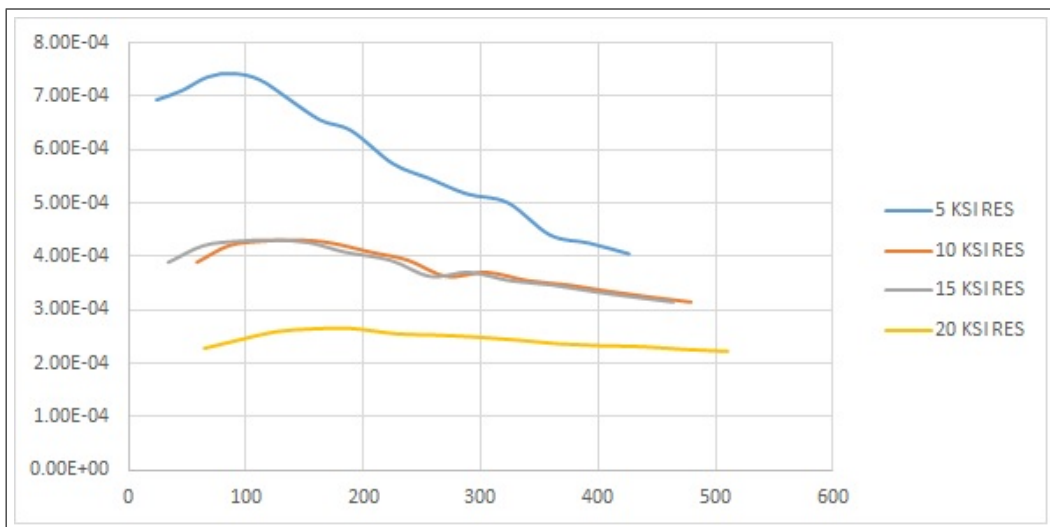

Figure 5.12: Resistance (in ohms) vs. current (in amps) at different contact pressures for rough rusted iron piece.
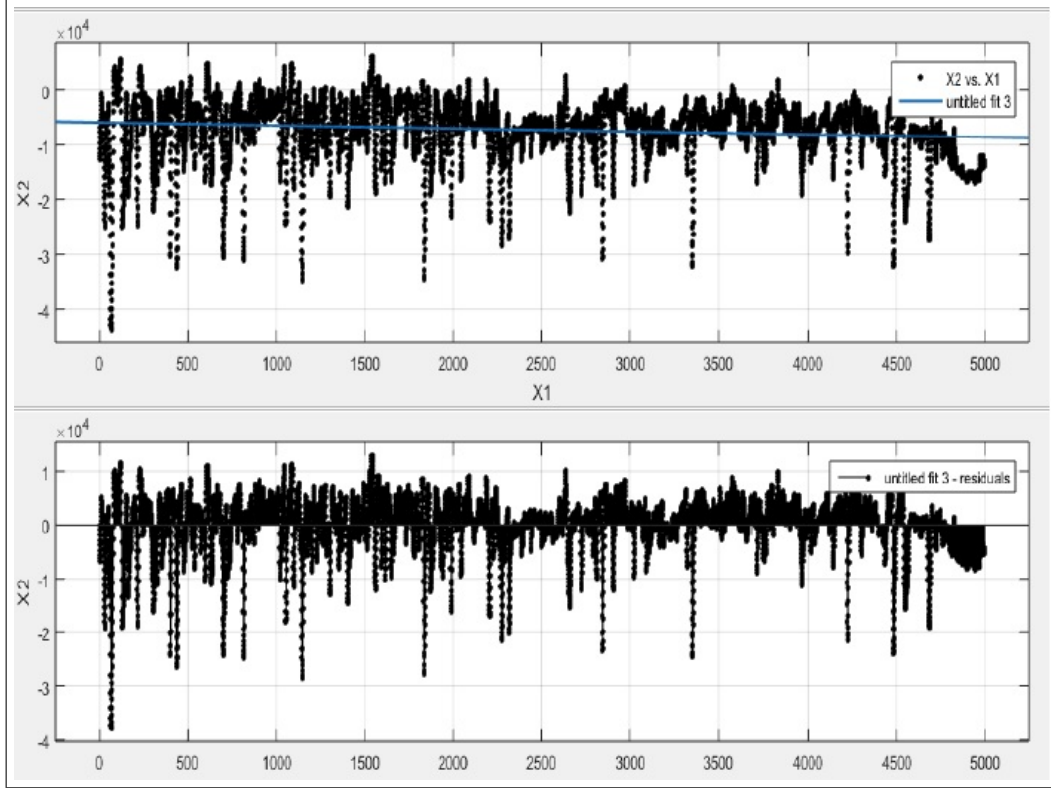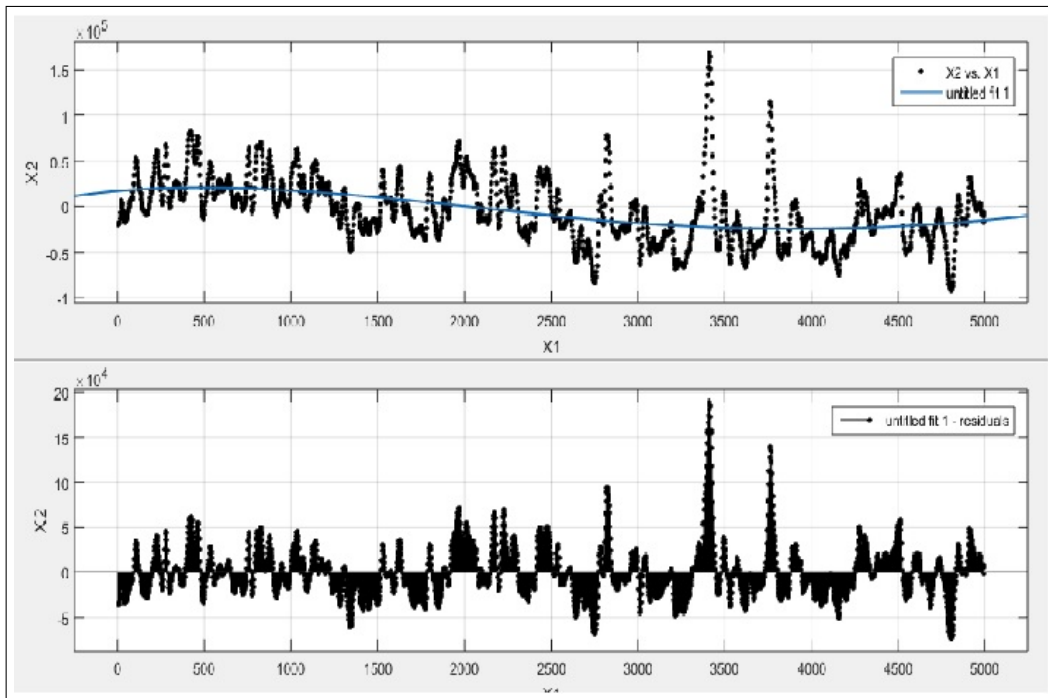
Figure 5.13: Surface plot of the rough rusted iron piece in X direction. The bottom plot filters out slight curvature in the top plot.
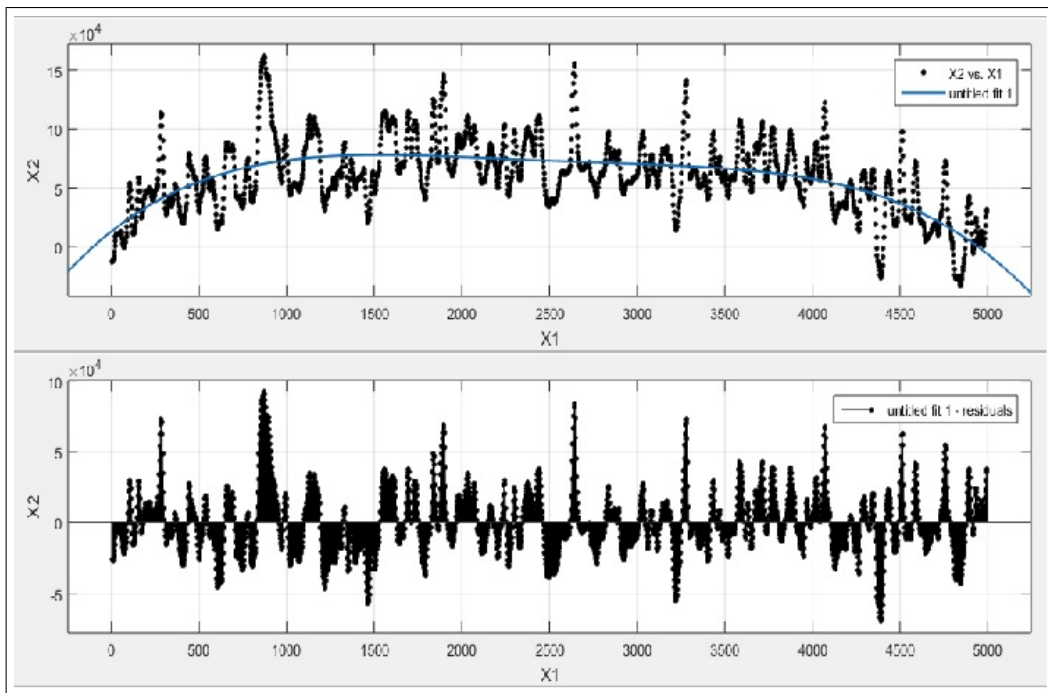
Figure 5.14: Surface plot of the rough rusted iron piece in Y direction. The bottom plot filters out the convex curvature in the top plot.

R_{RMS}(forging) (in horizontal direction) = 28872.67 Å
R_{RMS}(forging) (in longitudinal direction) = 31751.33 Å

5.1.4   Discussion on the Contact Resistance Test Results

From the plots of the contact resistances (Figures 5.2, 5.8 and 5.12) it can be seen that as the external contact pressure is increased, the contact resistance decreases. Moreover from Figures 5.1, 5.7 and 5.11, a somewhat inverse relation between the contact temperature and contact resistance is evident. This can be due to the asperity melting in the contact region leading to increased surface area resulting in reduced contact resistance [8]. Numerically, the contact resistance values obtained from the contact resistance test for all three different surface conditions are very low. The highest contact resistance at rated pressure (10 ksi) was around $400*10^{-6}$ Ω for the rusted iron piece. This implies that even if a very high fault current of say 100 kA were to flow through the contact, the voltage developed across it would be just 40 V, which is much less than the minimum voltage required for arcing, i.e. 300 V. This means that sparking cannot be the mechanism which leads to the arc marks in the retaining ring.

5.2   Transient FEA Simulation Results

The transient FEA simulation was run for 3 electrical cycles and the resistivity of the Contact2 region was changed at the instant t = 0.01041666666 sec from $4000*10^{-6}$ Ω–m to 50 Ω–m. The plot data from FLUX was exported to Microsoft Excel and the curves were plotted again in Excel for a clear plot. The voltage (VC2) across and current (IC2) through the Contact2 region were plotted as shown in Figure 5.15. Figure 5.16 zooms in on the plot of Figure 5.15 near the time of opening of contact (i.e. 10.41666666 ms). Figure 5.17 shows the current through the two contact regions, Contact and Contact2. The current density distribution before and after opening the contact can be seen in Figures 5.18 and 5.19. The skin effect due to high frequency is evident in these figures.
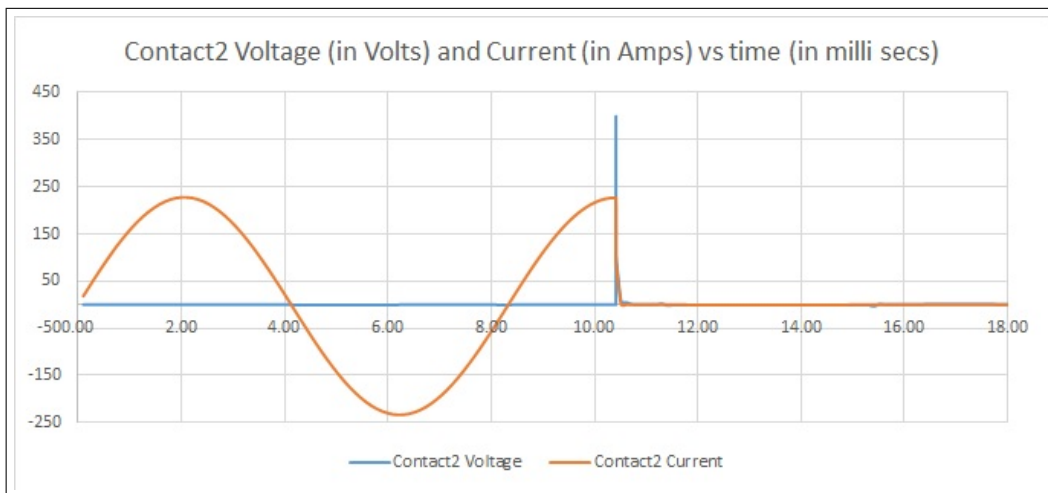
Figure 5.15: Voltage, VC2, across and current, IC2, through Contact2 region.
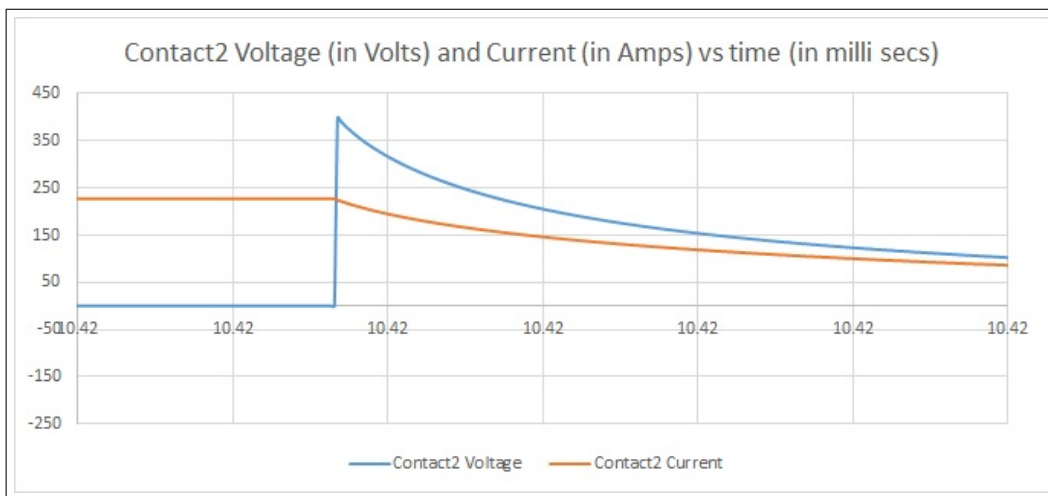
Figure 5.16: Zoomed-in voltage, VC2, across and current, IC2, through the Contact2 region near the instant of contact opening.
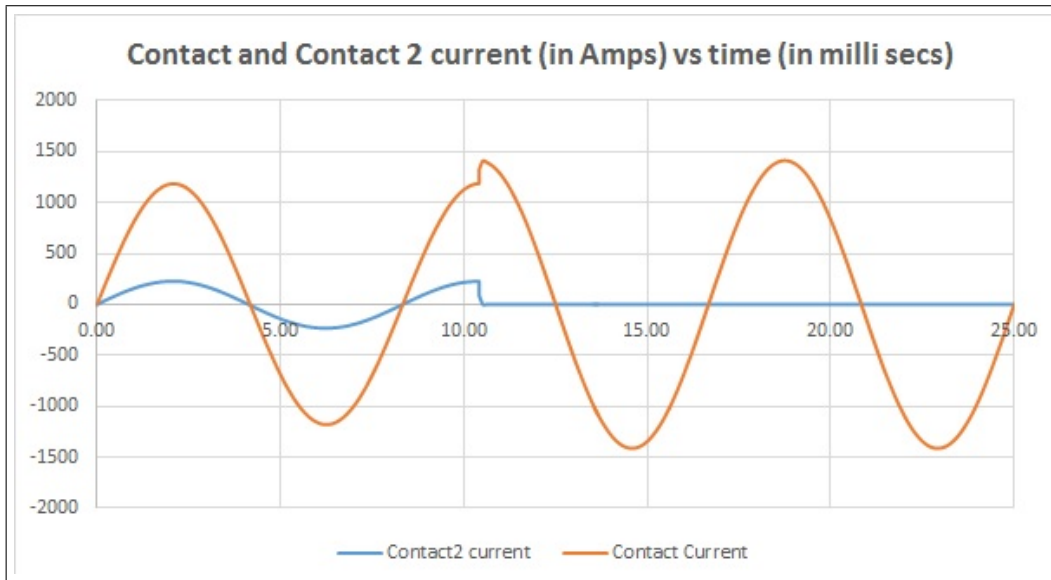
Figure 5.17: Current passing through Contact2 and Contact region (shown as surface S1).
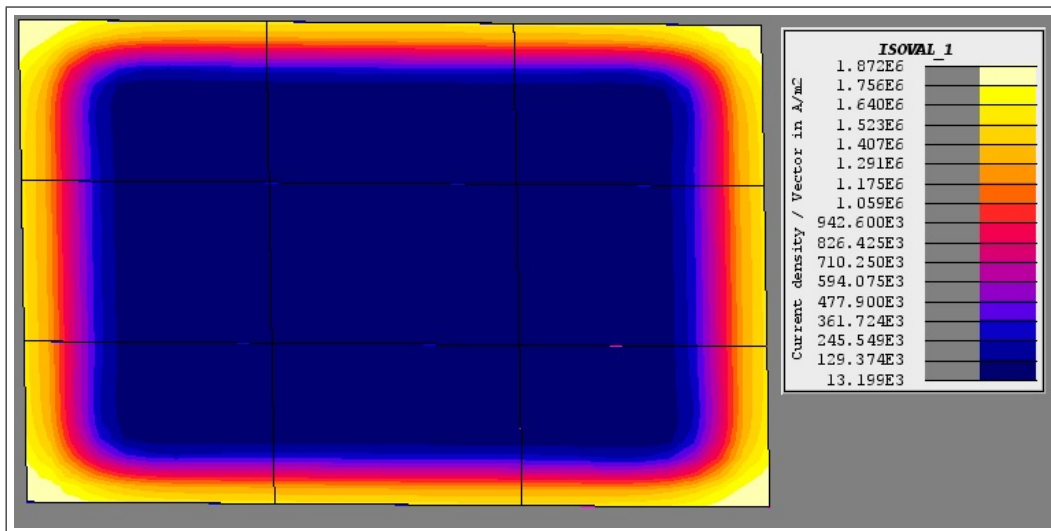
Figure 5.18: Current distribution in the whole contact region before Contact2 was opened. Due to the skin effect, the majority of current remains in the periphery.
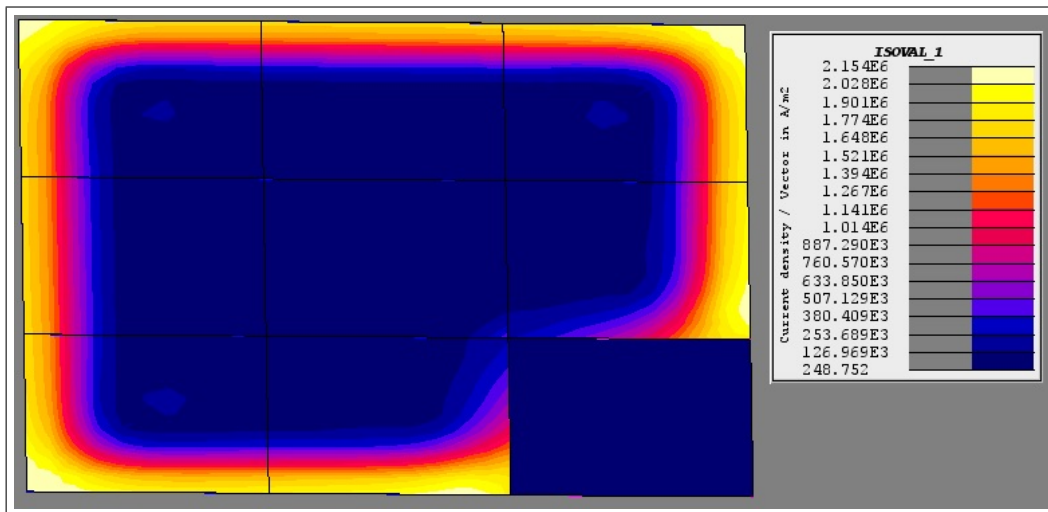
Figure 5.19: Current distribution in the whole contact region after Contact2 was opened.
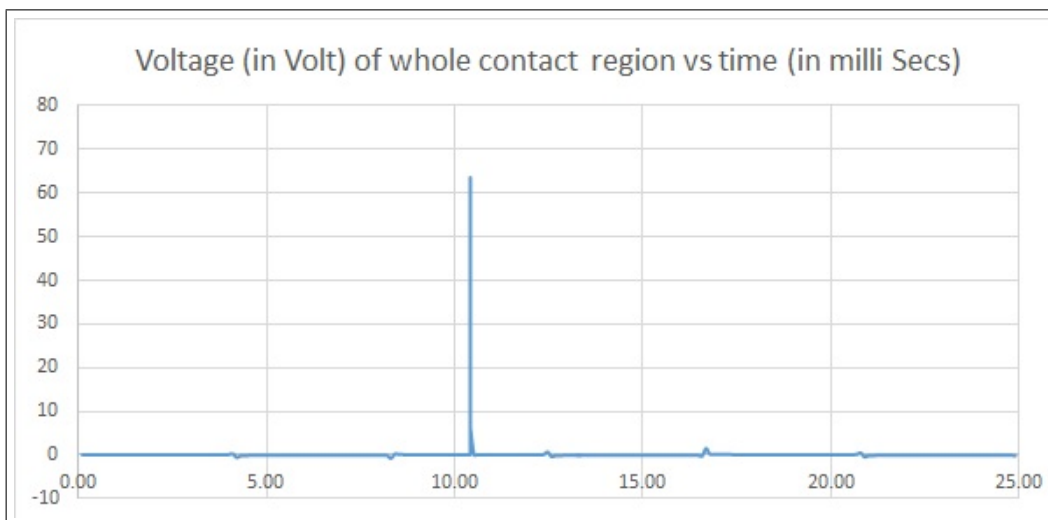
Figure 5.20: Voltage of the whole contact region (Contact+Contact2).

5.2.1 Discussion on the FEA Simulation Results

From Figures 5.15 and 5.16 it can be seen that when the resistance of the Contact2 region changes, the contact2 voltage increases to around 390 V. It is important to note that this is just a localized increase in the voltage of the Contact2 region. The voltage of the complete region ((Contact + Contact2) region) increases by a small amount comparatively, as shown in Figure 5.20. This voltage increase is because of the inherent inductance of the system, which tries to maintain the flow of the same amount of current as before and in the process produces a large transient voltage rise (equal to Ldi/dt). The voltage rise is well above 300 V and this will lead to the breakdown of the medium as per Paschen's law (Figure 2.7). This minimum value of breakdown voltage for hydrogen medium corresponds to a P*d (pressure times distance) value of around 2 torr–cm. The typical hydrogen pressure inside the generator is around 4 kg/cm^2, which for 2 torr–cm corresponds to 6.8 μm, which is the typical size of asperities in the contact region and also the gap between the two surfaces in that region [8]. Thus a make-and-break contact does have the possibility to arc even when relatively little current is flowing through the contact region (in this case it was demonstrated that 1 kA is enough for arcing).

CHAPTER 6

SCOPE OF FUTURE WORK

An experiment can be performed to recreate arcing in the laboratory. The vibration will be a periodic motion at 120 Hz frequency simulating the 120 Hz pulsating torque present in the machine. This will provide hard evidence that arcing in the retaining ring is mostly a make-and-break contact phenomenon.

The hardware tests performed to measure the contact resistance can be reperformed with actual rotor forging sample from the generator. This will give a more realistic values for contact resistance.

In the simulation the rotor steel and the retaining ring were assumed to be magnetically linear and as such saturation of the steel was ignored. This was done to get the first–order approximation and simplify the simulation. Saturation of the non-linear steel will lead to additional losses inside the rotor. However, this will not affect the losses in the contact region much, which is what is used for voltage drop calculation across the air-gap. The simulation can be performed again with modified material properties taking non-linearity into account for more accuracy.

Arcing in the retaining ring also occurs with the slot wedges. Wedges carry almost 90% of the current induced on the rotor because their materials have higher conductivity [7]. As such, wedge to retaining ring contact resistance is an important parameter which can provide important information about wedge and ring arcing. An experiment similar to what has been performed in this study can be performed involving retaining ring, rotor forging and slot wedges.

The peculiar predominance of arcing in Australia and New-Zealand has not been explored in this study. Further work is needed to pinpoint the exact reasons for the same.

CHAPTER 7

CONCLUSION

Retaining rings are the most highly stressed component of the entire turbo-generator system. As such, the tolerances for any defects or flaws are very small. Any small crack in the ring can lead quickly to full blown damage. The older 18-5 retaining rings were highly prone to stress corrosion cracking (SCC) and were consequently replaced by corrosion–resistant 18-18 rings in most of the generators around the world nearly 2 decades ago.

An industry survey assessing performance of these newly installed 18-18 rings identified arcing as a major problem. Arcing was found mostly in the retaining ring shrink fit region with teeth and wedge. Arcing was also found to be peculiarly predominant in certain geographic locations. In this thesis work, we analyzed different possible mechanisms which can lead to arcing and determined which mechanism is most likely based on hardware experiment, simulation and industry survey data.

The hardware experiment was performed to get contact resistance values typical in the shrink fit region between the retaining ring and the rotor forging at different contact pressure values. The resistance values obtained were very low and indicated that even very high fault currents cannot possibly produce the minimum voltage required for the voltage breakdown of the surrounding medium. This ruled out sparking or high voltage arcing as a possible mechanism.

Following the hardware experiment we tried to see if a make-and-break contact type arcing could be possible in the retaining ring. To explore this, a finite–element simulation was done in which a localized contact opening was simulated while the current was passing through contact region. This led to a localized voltage increase sufficient to cause arcing in the contact region. This voltage increase was the result of the inherent inductance in the system, leading to L*di/dt rise. It was interesting to note that a voltage increase of about 400 V was observed even though the current value was relatively small,

about 1000 A.

The making and breaking of contact can occur due to the slippage of the retaining ring over the rotor forging. The negative sequence currents resulting from the negative sequence component of the unbalanced stator current flow on the surface of the rotor forging due to the small skin depth. The small skin depth also leads to very high resistance, which leads to high resistive losses. The heat produced due to these losses in the shrink fit region leads to reduction in the shrink-fit pressure which loosens the shrink fit. In addition, these double frequency currents generate pulsating torque, which leads to vibration in the retaining ring. This vibration, combined with the heat, leads to small slippage of the retaining ring over the rotor forging. The fretting marks observed in the shrink fit region in the retaining ring survey [3] provide evidence of such slippage. This slippage leads to loss of some of the current–carrying contacts and cause a transient localized voltage shoot which can produce arcing.

More hardware experiments need to be done to get hard evidence of arcing due to make-and-break contact in the shrink fit region. More research is needed to pinpoint the exact reasons of peculiar predominance of arcing in the Australasian region.

APPENDIX A

MEASUREMENT DATA FOR CONTACT RESISTANCE TEST WITH SMOOTH IRON SURFACE

Table A.1: Experimental data for contact resistance test with smooth iron surface at 0 external pressure

EXPERIMENT SET 1: NO PRESSURE APPLIED, AMBIENT 22.1 DEG C, HUMIDITY 59% (OUTSIDE THE LAB),								
ALL VOLTAGES IN VOLTS, CURRENTS IN AMPS, ANGLES IN DEGREES AND TEMPERATURES IN DEG C								
S. No.	VOLTAGE TO UPC	I/P VOLTAGE	I/P CURRENT	CONTACT VOLTAGE	CONTACT CURRENT	PHASE DIFF	O/P CT VOLTAGE	TEMP1	TEMP2
1	10	10.177	1.79E-02	3.02E-02	3.6	LOW SIGNAL	20.22 E-3	22.1	22.1
2	20	20.176	3.26E-02	5.99E-02	7.3	1	3.90E-02	2.22E+01	2.22E+01
3	30	30.172	4.77E-02	8.94E-02	11.4	1.2	5.80E-02	2.22E+01	2.23E+01
4	40	40.18	7.74E-02	1.13E-01	20.2	1.6	9.86E-02	2.24E+01	2.27E+01
5	50	50.19	1.35E-01	1.34E-01	38	3	1.84E-01	2.28E+01	2.38E+01
6	60	60.22	2.29E-01	1.48E-01	66.9	0.4	3.21E-01	2.32E+01	2.60E+01
7	70	70.25	3.26E-01	1.61E-01	97.4	1.6	4.68E-01	2.43E+01	2.82E+01
8	80	80.24	4.28E-01	1.71E-01	129.3	1	6.18E-01	2.59E+01	3.04E+01
9	90	90.26	5.31E-01	1.82E-01	161	2	7.73E-01	2.84E+01	3.34E+01
10	100	100.27	6.32E-01	1.93E-01	192	2	9.22E-01	3.06E+01	3.56E+01
11	110	110.32	7.30E-01	2.06E-01	227	3	1.06E+00	3.25E+01	3.85E+01
12	120	120.32	7.58E-01	2.33E-01	237	3	1.10E+00	3.42E+01	4.20E+01
13	130	130.3	8.10E-01	2.57E-01	250	2.5	1.16E+00	3.57E+01	4.39E+01
14	140	140.31	9.00E-01	2.79E-01	265	2	1.23E+00	3.78E+01	4.69E+01
15	150	150.3	1.27E+00	2.98E-01	287	3	1.34E+00	4.00E+01	5.08E+01

Table A.2: Experimental data for contact resistance test with smooth iron surface at 0 external pressure

| | EXPERIMENT SET 2: 27.8KIPS FORCE APPLIED, AMBIENT 22.1 DEG C, HUMIDITY 59% (OUTSIDE THE LAB), | | | | | | | | |
| | *ALL VOLTAGES IN VOLTS, CURRENTS IN AMPS, ANGLES IN DEGREES AND TEMPERATURES IN DEG C* | | | | | | | | |
S. No.	VOLTAGE TO UPC	I/P VOLTAGE	I/P CURRENT	O/P VOLTAGE	O/P CURRENT	PHASE DIFF	O/P CT VOLTAGE	TEMP1	TEMP2
1	20	20.158	2.57E-01	5.54E-03	78.9	-143.2	3.93E-01	3.15E+01	2.90E+01
2	30	30.15	3.77E-01	8.60E-03	116.6	-146	5.61E-01	3.13E+01	2.89E+01
3	40	40.15	4.99E-01	1.14E-02	155	-149.5	7.45E-01	3.12E+01	2.89E+01
4	50	50.15	6.23E-01	1.39E-02	194.3	-150	9.32E+02	3.12E+01	2.89E+01
5	60	60.19	7.50E-01	1.62E-02	241	-151	1.12E+00	3.13E+01	2.90E+01
6	70	70.21	8.77E-01	1.84E-02	283	-151.3	1.32E+00	3.15E+01	2.90E+01
7	80	80.2	1.00E+00	2.10E-02	325	-151.6	1.52E+00	3.18E+01	2.91E+01
8	90	90.22	1.14E+00	2.30E-02	367	-151.4	1.71E+00	3.21E+01	2.93E+01
9	100	100.24	1.27E+00	2.48E-02	410	-151.5	1.90E+00	3.25E+01	2.95E+01
10	110	110.29	1.40E+00	2.50E-02	453	-151.7	2.11E+00	3.31E+01	2.96E+01
11	120	120.28	1.54E+00	2.91E-02	495	-152.2	2.30E+00	3.44E+01	3.00E+01
12	130	130.26	1.69E+00	3.07E-02	537	-152	2.51E+00	3.50E+01	3.03E+01
13	140	140.24	1.87E+00	3.04E-02	579	-152.2	2.70E+00	3.59E+01	3.07E+01
14	150	150.22	2.33E+00	3.01E-02	621	-151.6	2.92E+00	3.69E+01	3.11E+01

Table A.3: Experimental data for contact resistance test with smooth iron surface at 10 ksi external pressure

| | EXPERIMENT SET 3: 55.1 KIPS FORCE APPLIED, AMBIENT 22.1 DEG C, HUMIDITY 59% (OUTSIDE THE LAB), | | | | | | | | |
| | *ALL VOLTAGES IN VOLTS, CURRENTS IN AMPS, ANGLES IN DEGREES AND TEMPERATURES IN DEG C* | | | | | | | | |
S. No.	VOLTAGE TO UPC	I/P VOLTAGE	I/P CURRENT	O/P VOLTAGE	O/P CURRENT	PHASE DIFF	O/P CT VOLTAGE	TEMP1	TEMP2
1	10	10.166	1.39E-01	2.30E-03	41.8	LOW SIGNAL	2.03E+02	3.52E+01	3.08E+01
2	20	20.158	2.58E-01	4.20E-03	79.3	49.9	3.90E-01	3.49E+01	3.06E+01
3	30	30.15	3.78E-01	6.36E-03	117.2	42	5.68E-01	3.48E+01	3.09E+01
4	40	40.152	4.99E-01	8.30E-03	155.6	38	7.49E-01	3.47E+01	3.08E+01
5	50	50.163	6.23E+02	9.92E-03	194.9	3.77E+01	9.35E-01	3.47E+01	3.06E+01
6	60	60.2	7.49E-01	1.20E-02	242	34	1.13E+00	3.47E+01	3.09E+01
7	70	70.225	8.77E-01	1.47E-02	284	33.5	1.32E+00	3.48E+01	3.08E+01
8	80	80.22	1.00E+00	1.77E-02	325	34	1.51E+00	3.50E+01	3.11E+01
9	90	90.24	1.14E+00	1.87E-02	367	34	1.72E+00	3.52E+01	3.09E+01
10	100	100.26	1.26E+00	2.05E-02	410	34.2	1.91E+00	3.55E+01	3.11E+01
11	110	110.31	1.40E+00	2.30E-02	452	32	2.11E+00	3.58E+01	3.13E+01
12	120	120.32	1.54E+00	2.25E-02	494	34.5	2.31E+00	3.64E+01	3.15E+01
13	130	130.3	1.69E+00	2.24E-02	536	34.5	2.51E+00	3.70E+01	3.16E+01
14	140	140.3	1.87E+00	2.39E-02	578	33	2.72E+00	3.76E+01	3.20E+01
15	150	150.27	2.33E+00	2.58E-02	621	35.5	2.92E+00	3.85E+01	3.24E+01

Table A.4: Experimental data for contact resistance test with smooth iron surface at 15 ksi external pressure

S. No.	VOLTAGE TO UPC	I/P VOLTAGE	I/P CURRENT	O/P VOLTAGE	O/P CURRENT	PHASE DIFF	O/P CT VOLTAGE	TEMP1	TEMP2
	EXPERIMENT SET 4: 82.7 KIPS FORCE APPLIED, AMBIENT 22.1 DEG C, HUMIDITY 59% (OUTSIDE THE LAB),								
	ALL VOLTAGES IN VOLTS, CURRENTS IN AMPS, ANGLES IN DEGREES AND TEMPERATURES IN DEG C								
1	10	10.16	1.38E-01	1.85E-03	41.8	LOW SIGNAL	2.07E-01	3.74E+01	3.25E+01
2	20	20.16	2.57E-01	3.90E-03	79.1	48	3.83E-01	3.73E+01	3.25E+01
3	30	30.15	3.76E-01	6.20E-03	116.7	42	5.60E-01	3.72E+01	3.25E+01
4	40	40.15	4.97E-01	8.00E-03	155	39	7.43E-01	3.72E+01	3.25E+01
5	50	50.158	6.20E+02	1.05E-02	194	3.50E+01	9.30E-01	3.72E+01	3.26E+01
6	60	60.199	7.47E-01	1.26E-02	241	35	1.13E+00	3.72E+01	3.22E+01
7	70	70.22	8.75E-01	1.40E-02	283	35	1.32E+00	3.73E+01	3.23E+01
8	80	80.22	1.00E+00	1.46E-02	324	35	1.52E+00	3.74E+01	3.27E+01
9	90	90.23	1.13E+00	1.62E-02	367	34.6	1.71E+00	3.76E+01	3.28E+01
10	100	100.26	1.27E+00	1.85E-02	410	33	1.91E+00	3.79E+01	3.30E+01
11	110	110.31	1.40E+00	2.24E-02	451	33	2.11E+00	3.84E+01	3.30E+01
12	120	120.31	1.53E+00	2.29E-02	492	33	2.31E+00	3.90E+01	3.35E+01
13	130	130.28	1.68E+00	2.50E-02	534	34	2.51E+00	3.95E+01	3.38E+01
14	140	140.26	1.86E+00	2.61E-02	576	34	2.70E+00	4.02E+01	3.39E+01
15	150	150.23	2.33E+00	2.92E-02	619	34	2.91E+00	4.10E+01	3.44E+01

Table A.5: Experimental data for contact resistance test with smooth iron surface at 20 ksi external pressure

S. No.	VOLTAGE TO UPC	I/P VOLTAGE	I/P CURRENT	O/P VOLTAGE	O/P CURRENT	PHASE DIFF	O/P CT VOLTAGE	TEMP1	TEMP2
	EXPERIMENT SET 5: 110.2 KIPS FORCE APPLIED, AMBIENT 22.1 DEG C, HUMIDITY 59% (OUTSIDE THE LAB),								
	ALL VOLTAGES IN VOLTS, CURRENTS IN AMPS, ANGLES IN DEGREES AND TEMPERATURES IN DEG C								
1	10	10.16	1.37E-01	2.00E-03	41.5	LOW SIGNAL	2.05E-01	3.88E+01	3.43E+01
2	20	20.15	2.56E-01	4.40E-03	78.6	47	3.70E-01	3.85E+01	3.43E+01
3	30	30.14	3.74E-01	7.14E-03	116	41	5.59E-01	3.84E+01	3.42E+01
4	40	40.14	4.94E-01	9.59E-03	153.7	39	7.39E-01	3.82E+01	3.42E+01
5	50	50.145	6.17E-01	1.19E-02	192.5	3.70E+01	9.24E-01	3.82E+01	3.42E+01
6	60	60.18	7.41E-01	1.37E-02	239	37	1.12E+00	3.81E+01	3.41E+01
7	70	70.2	8.68E-01	1.61E-02	280	37	1.31E+00	3.82E+01	3.40E+01
8	80	80.2	9.96E-01	1.79E-02	322	34	1.50E+00	3.82E+01	3.40E+01
9	90	90.21	1.12E+00	1.97E-02	363	33	1.70E+00	3.84E+01	3.43E+01
10	100	100.23	1.25E+00	1.99E-02	405	34.29	1.89E+00	3.87E+01	3.45E+01
11	110	110.28	1.39E+00	2.03E-02	446	33	2.10E+00	3.91E+01	3.45E+01
12	120	120.28	1.52E+00	2.40E-02	488	37	2.21E+00	3.95E+01	3.47E+01
13	130	130.25	1.67E+00	2.63E-02	530	33	2.50E+00	3.99E+01	3.49E+01
14	140	140.25	1.85E+00	2.79E-02	572	34.33	2.70E+00	4.04E+01	3.51E+01
15	150	150.21	2.31E+00	2.83E-02	615	35	2.90E+00	4.10E+01	3.52E+01

APPENDIX B

MEASUREMENT DATA FOR CONTACT RESISTANCE TEST WITH ROUGH IRON SURFACE

Table B.1: Experimental data for contact resistance test with rough iron surface at 0 external pressure

EXPERIMENT SET 1: NO PRESSURE APPLIED, AMBIENT 22.1 DEG C, HUMIDITY 59% (OUTSIDE THE LAB),									
ALL VOLTAGES IN VOLTS, CURRENTS IN AMPS, ANGLES IN DEGREES AND TEMPERATURES IN DEG C									
S. No.	VOLTAGE TO UPC	I/P VOLTAGE	I/P CURRENT	O/P VOLTAGE	O/P CURRENT	PHASE DIFF	O/P CT VOLTAGE	TEMP1	TEMP2
1	10	10.17	6.35E-02	2.00E-02	18.6	0	9.00E-02	36.2	39.4
2	20	20.166	1.21E-02	3.94E-02	36	1	1.76E-01	3.61E+01	3.93E+01
3	30	30.15	1.75E-01	5.94E-02	52.3	1.6	2.60E-01	3.62E+01	3.93E+01
4	40	40.16	2.26E-01	8.00E-02	68	1.4	3.34E-01	3.63E+01	3.93E+01
5	50	50.17	2.72E-01	1.02E-01	82.1	1.3	4.00E-01	3.66E+01	3.95E+01
6	60	60.217	3.20E-01	1.24E-01	96.5	1	4.80E-01	3.68E+01	3.97E+01
7	70	70.24	3.82E-01	1.42E-01	115.6	2	5.77E-01	3.72E+01	3.99E+01
8	80	80.23	4.18E-01	1.66E-01	126.4	2	6.22E-01	3.76E+01	4.04E+01
9	90	90.25	4.88E-01	1.83E-01	148	1	7.30E-01	3.84E+01	4.13E+01
10	100	100.26	5.57E-01	1.99E-01	169	2	8.40E-01	3.91E+01	4.24E+01
11	110	110.31	6.17E-01	2.19E-01	187	1	9.29E-01	3.99E+01	4.38E+01
12	120	120.32	6.80E-01	2.39E-01	211	1.5	1.02E+00	4.05E+01	4.48E+01
13	130	130.3	7.60E-01	2.59E-01	230	1.8	1.10E+00	4.15E+01	4.63E+01
14	140	140.31	7.70E-01	2.99E-01	225	1.2	1.08E+00	4.25E+01	4.84E+01
15	150	150.3	1.20E+00	3.11E-01	253	1.1	1.23E+00	4.32E+01	5.06E+01

Table B.2: Experimental data for contact resistance test with rough iron surface at 5 ksi external pressure

	EXPERIMENT SET 2: 27.8KIPS FORCE APPLIED, AMBIENT 22.1 DEG C, HUMIDITY 59% (OUTSIDE THE LAB),								
	ALL VOLTAGES IN VOLTS, CURRENTS IN AMPS, ANGLES IN DEGREES AND TEMPERATURES IN DEG C								
S. No.	VOLTAGE TO UPC	I/P VOLTAGE	I/P CURRENT	O/P VOLTAGE	O/P CURRENT	PHASE DIFF	O/P CT VOLTAGE	TEMP1	TEMP2
1	20	20.157	2.40E-01	3.30E-03	74.4	17	3.70E-01	3.20E+01	3.35E+01
2	30	30.14	3.53E-01	5.37E-03	110.1	15	5.50E-01	3.19E+01	3.33E+01
3	40	40.13	4.67E-01	7.45E-03	146	13	7.31E-01	3.18E+01	3.32E+01
4	50	50.14	5.82E-01	9.46E-03	182.3	13	9.05E-01	3.18E+01	3.31E+01
5	60	60.17	6.98E-01	1.14E-02	226	12	1.09E+00	3.17E+01	3.31E+01
6	70	70.19	8.14E-01	1.32E-02	263	11	1.25E+00	3.17E+01	3.32E+01
7	80	80.18	9.32E-01	1.50E-02	301	12	1.45E+00	3.18E+01	3.33E+01
8	90	90.2	1.05E+00	1.67E-02	340	10	1.64E+00	3.19E+01	3.34E+01
9	100	100.22	1.18E+00	1.84E-02	380	10	1.84E+00	3.20E+01	3.37E+01
10	110	110.26	1.30E+00	2.01E-02	419	10	2.03E+00	3.20E+01	3.40E+01
11	120	120.25	1.43E+00	2.17E-02	459	9.5	2.23E+00	3.23E+01	3.44E+01
12	130	130.23	1.57E+00	2.32E-02	499	10	2.43E+00	3.25E+01	3.49E+01
13	140	140.22	1.75E+00	2.48E-02	539	10	2.63E+00	3.28E+01	3.55E+01
14	150	150.23	2.25E+00	2.64E-02	581	8	2.85E+00	3.31E+01	3.60E+01

Table B.3: Experimental data for contact resistance test with rough iron surface at 10 ksi external pressure

	EXPERIMENT SET 3: 55.1 KIPS FORCE APPLIED, AMBIENT 22.1 DEG C, HUMIDITY 59% (OUTSIDE THE LAB),								
	ALL VOLTAGES IN VOLTS, CURRENTS IN AMPS, ANGLES IN DEGREES AND TEMPERATURES IN DEG C								
S. No.	VOLTAGE TO UPC	I/P VOLTAGE	I/P CURRENT	O/P VOLTAGE	O/P CURRENT	PHASE DIFF	O/P CT VOLTAGE	TEMP1	TEMP2
1	10	low signal	low signal	low signal	low signal	low signal	low signal	low signal	low signal
2	20	20.159	2.43E-01	2.70E-03	74.9	19	3.70E-01	3.27E+01	3.51E+01
3	30	30.147	3.56E-01	4.70E-03	110.2	19	5.48E-01	3.26E+01	3.50E+01
4	40	40.145	4.67E-01	6.72E-03	145.7	15	7.30E-01	3.26E+01	3.50E+01
5	50	50.15	5.82E-01	8.60E-03	181.8	1.50E+01	9.00E-01	3.26E+01	3.50E+01
6	60	60.18	6.98E-01	1.04E-02	225	12.5	1.09E+00	3.26E+01	3.50E+01
7	70	70.2	8.15E-01	1.21E-02	262	12	1.28E+00	3.26E+01	3.50E+01
8	80	80.2	9.32E-01	1.37E-02	300	12	1.46E+00	3.26E+01	3.50E+01
9	90	90.21	1.05E+00	1.51E-02	339	10	1.64E+00	3.27E+01	3.52E+01
10	100	100.23	1.17E+00	1.67E-02	377	10	1.83E+00	3.29E+01	3.53E+01
11	110	110.28	1.29E+00	1.81E-02	417	10	2.02E+00	3.30E+01	3.56E+01
12	120	120.28	1.42E+00	1.96E-02	456	10	2.21E+00	3.31E+01	3.58E+01
13	130	130.25	1.56E+00	2.09E-02	496	10.5	2.41E+00	3.34E+01	3.63E+01
14	140	140.25	1.74E+00	2.22E-02	536	10	2.61E+00	3.35E+01	3.67E+01
15	150	150.24	2.24E+00	2.36E-02	577	10	8.30E-01	3.39E+01	3.73E+01

Table B.4: Experimental data for contact resistance test with rough iron surface at 15 ksi external pressure

EXPERIMENT SET 4: 82.7 KIPS FORCE APPLIED, AMBIENT 22.1 DEG C, HUMIDITY 59% (OUTSIDE THE LAB),								
ALL VOLTAGES IN VOLTS, CURRENTS IN AMPS, ANGLES IN DEGREES AND TEMPERATURES IN DEG C								
S. No.	VOLTAGE TO UPC	I/P VOLTAGE	I/P CURRENT	O/P VOLTAGE	O/P CURRENT	PHASE DIFF	O/P CT VOLTAGE	TEMP1	TEMP2
1	10	low signal	low signal	low signal	low signal	low signal	low signal	low signal	low signal
2	20	low signal							
3	30	30.145	3.52E-01	4.44E-03	109.2	20	5.33E-01	3.38E+01	3.68E+01
4	40	40.14	4.64E-01	6.34E-03	144.4	16	7.13E-01	3.37E+01	3.68E+01
5	50	50.14	5.77E-01	8.22E-03	180.1	1.40E+01	8.90E-01	3.37E+01	3.68E+01
6	60	60.17	6.93E-01	9.92E-03	223	14	1.08E+00	3.37E+01	3.67E+01
7	70	70.19	8.10E-01	1.15E-02	261	12	1.27E+00	3.38E+01	3.67E+01
8	80	80.18	9.28E-01	1.30E-02	298	1.20E+01	1.45E+00	3.38E+01	3.68E+01
9	90	90.19	1.05E+00	1.45E-02	337	12	1.64E+00	3.38E+01	3.69E+01
10	100	100.22	1.16E+00	1.60E-02	375	12	1.84E+00	3.40E+01	3.70E+01
11	110	110.26	1.28E+00	1.73E-02	414	11	2.02E+00	3.42E+01	3.73E+01
12	120	120.25	1.42E+00	1.87E-02	454	11	2.20E+00	3.43E+01	3.78E+01
13	130	130.24	1.55E+00	2.00E-02	493	11	2.40E+00	3.46E+01	3.81E+01
14	140	140.24	1.73E+00	2.14E-02	533	11	2.60E+00	3.48E+01	3.85E+01
15	150	150.24	2.23E+00	2.26E-02	575	11	2.82E+00	3.51E+01	3.92E+01

Table B.5: Experimental data for contact resistance test with rough iron surface at 20 ksi external pressure

EXPERIMENT SET 5: 110.2 KIPS FORCE APPLIED, AMBIENT 22.1 DEG C, HUMIDITY 59% (OUTSIDE THE LAB),								
ALL VOLTAGES IN VOLTS, CURRENTS IN AMPS, ANGLES IN DEGREES AND TEMPERATURES IN DEG C								
S. No.	VOLTAGE TO UPC	I/P VOLTAGE	I/P CURRENT	O/P VOLTAGE	O/P CURRENT	PHASE DIFF	O/P CT VOLTAGE	TEMP1	TEMP2
1	10	low signal							
2	20	low signal							
3	30	30.15	3.50E-01	4.45E-03	108.6	18	5.30E-01	3.53E+01	3.89E+01
4	40	40.14	4.60E-01	6.35E-03	143.6	17	7.00E-01	3.53E+01	3.89E+01
5	50	50.15	5.74E-01	8.10E-03	179.2	1.50E+01	8.90E-01	3.52E+01	3.89E+01
6	60	60.18	6.90E-01	9.80E-03	222	15	1.08E+00	3.52E+01	3.89E+01
7	70	70.2	8.06E-01	1.15E-02	260	14	1.26E+00	3.53E+01	3.89E+01
8	80	80.19	9.24E-01	1.29E-02	298	12	1.45E+00	3.53E+01	3.89E+01
9	90	90.21	1.04E+00	1.44E-02	336	12	1.64E+00	3.54E+01	3.90E+01
10	100	100.23	1.16E+00	1.58E-02	374	12	1.83E+00	3.55E+01	3.92E+01
11	110	110.27	1.28E+00	1.72E-02	413	11	2.00E+00	3.57E+01	3.94E+01
12	120	120.27	1.41E+00	1.84E-02	452	12	2.19E+00	3.58E+01	3.97E+01
13	130	130.25	1.55E+00	1.97E-02	491	12.3	2.39E+00	3.60E+01	4.00E+01
14	140	140.25	1.73E+00	2.10E-02	531	12	2.60E+00	3.62E+01	4.04E+01
15	150	150.24	2.23E+00	2.22E-02	573	11	2.81E+00	3.66E+01	4.10E+01
16	152	152.23	2.54	2.25E-02	580	11	2.85	36.9	41.5

APPENDIX C

MEASUREMENT DATA FOR CONTACT RESISTANCE TEST WITH ROUGH AND RUSTED IRON SURFACE

Table C.1: Experimental data for contact resistance test with rough and rusted iron surface at 1 ksi external pressure

EXPERIMENT SET 1: 1 ksi PRESSURE APPLIED, AMBIENT 22.1 DEG C, HUMIDITY 59% (OUTSIDE THE LAB)									
ALL VOLTAGES IN VOLTS, CURRENTS IN AMPS, ANGLES IN DEGREES AND TEMPERATURES IN DEG C									
S. No.	VOLTAGE TO UPC	I/P VOLTAGE	I/P CURRENT	O/P VOLTAGE	O/P CURRENT	PHASE DIFF	O/P CT VOLTAGE	TEMP1	TEMP2
1	10	10.176	1.40E-05	6.40E-02	5.3	178	2.60E-02	22.3	22.3
2	20	20.189	4.14E-02	8.20E-02	10.7	178	5.40E-02	2.22E+01	2.23E+01
3	30	29.454	6.22E-02	9.70E-02	16.4	179.7	8.20E-02	2.23E+01	2.23E+01
4	40	40.2	8.50E-02	1.22E-01	23	179.5	1.16E-01	2.23E+01	2.24E+01
5	50	50.18	1.35E-01	1.45E-01	35	179.6	1.75E-01	2.22E+01	2.26E+01
6	60	60.22	1.90E-01	1.56E-01	53.5	179.7	2.65E-01	2.22E+01	2.32E+01
7	70	70.19	2.75E-01	1.72E-01	80.3	179.2	3.95E-01	2.23E+01	2.39E+01
8	80	80.18	3.92E-01	1.77E-01	117.4	179	5.54E-01	2.23E+01	2.52E+01
9	90	90.18	5.35E-01	1.82E-01	161	178	7.90E-01	2.24E+01	2.68E+01
10	100	100.19	6.62E-01	1.81E-01	207	177.7	1.00E+00	2.25E+01	2.85E+01
11	110	110.22	7.77E-01	1.84E-01	245	179.1	1.15E+00	2.27E+01	2.97E+01
12	120	120.21	9.00E-01	1.90E-01	282	178	1.34E+00	2.28E+01	3.09E+01
13	130	130.19	1.00E+00	1.96E-01	318	176	1.53E+00	2.29E+01	3.23E+01
14	140	140.18	1.16E+00	2.00E-01	354	176	1.71E+00	2.29E+01	3.38E+01
15	150	150.31	1.54E+00	2.06E-01	390	175	1.87E+00	2.31E+01	3.52E+01

Table C.2: Experimental data for contact resistance test with rough and rusted iron surface at 5 ksi external pressure

EXPERIMENT SET 2: 27.8KIPS FORCE APPLIED, AMBIENT 22.1 DEG C, HUMIDITY 77% (OUTSIDE THE LAB),								
ALL VOLTAGES IN VOLTS, CURRENTS IN AMPS, ANGLES IN DEGREES AND TEMPERATURES IN DEG C								
S. No.	VOLTAGE TO UPC	I/P VOLTAGE	I/P CURRENT	O/P VOLTAGE	O/P CURRENT	PHASE DIFF	O/P CT VOLTAGE	TEMP1	TEMP2
1	10	10.158	0.013	1.68E-02	24	172.2	0.118	27.5	35.8
2	20	20.153	1.57E-01	3.28E-02	45.8	173	2.23E-01	2.94E+01	3.55E+01
3	30	30.143	2.24E-01	5.00E-02	67.1	171.2	3.30E-01	2.79E+01	3.55E+01
4	40	40.13	2.93E-01	6.67E-02	88.9	172	4.43E-01	2.91E+01	3.56E+01
5	50	50.11	3.64E-01	8.27E-02	111.8	171.4	5.59E-01	2.56E+01	3.57E+01
6	60	60.14	4.44E-01	9.62E-02	137	171.4	6.86E-01	2.92E+01	3.59E+01
7	70	70.15	5.25E-01	1.09E-01	163.5	171	8.12E-01	2.92E+01	3.62E+01
8	80	80.14	6.12E-01	1.23E-01	189.8	170	9.45E-01	2.95E+01	3.68E+01
9	90	90.15	7.05E-01	1.31E-01	225	170	1.00E+00	2.78E+01	3.74E+01
10	100	100.17	8.04E-01	1.42E-01	256	170	1.25E+00	2.77E+01	3.82E+01
11	110	110.21	9.02E-01	1.51E-01	288	169.8	1.41E+00	2.82E+01	3.90E+01
12	120	120.2	1.02E+00	1.64E-01	323	170	1.58E+00	3.17E+01	4.01E+01
13	130	130.18	1.13E+00	1.61E-01	359	170	1.75E+00	3.18E+01	4.45E+01
14	140	140.17	1.27E+00	1.69E-01	392	170	1.90E+00	3.20E+01	4.54E+01
15	150	150.15	1.66E+00	1.75E-01	426	170	2.08E+00	3.24E+01	4.62E+01

Table C.3: Experimental data for contact resistance test with rough and rusted iron surface at 10 ksi external pressure

EXPERIMENT SET 3: 55.1 KIPS FORCE APPLIED, AMBIENT 22.1 DEG C, HUMIDITY 59% (OUTSIDE THE LAB),								
ALL VOLTAGES IN VOLTS, CURRENTS IN AMPS, ANGLES IN DEGREES AND TEMPERATURES IN DEG C								
S. No.	VOLTAGE TO UPC	I/P VOLTAGE	I/P CURRENT	O/P VOLTAGE	O/P CURRENT	PHASE DIFF	O/P CT VOLTAGE	TEMP1	TEMP2
1	10	low signal							
2	20	20.148	1.95E-01	2.36E-02	58.3	164.3	2.83E-01	2.66E+01	3.13E+01
3	30	30.134	2.81E-01	3.70E-02	85.4	166	4.24E-01	2.67E+01	3.13E+01
4	40	40.11	3.68E-01	5.00E-02	113.1	166	5.80E-01	2.66E+01	3.14E+01
5	50	50.1	4.58E-01	6.29E-02	141.5	1.66E+02	7.07E-01	2.66E+01	3.14E+01
6	60	60.13	5.52E-01	7.50E-02	170.8	166	8.58E-01	2.66E+01	3.18E+01
7	70	70.14	6.47E-01	8.67E-02	207	167	1.00E+00	2.65E+01	3.23E+01
8	80	80.12	7.45E-01	9.64E-02	238	166	1.16E+00	2.66E+01	3.28E+01
9	90	90.13	8.45E-01	1.01E-01	271	167	1.32E+00	2.68E+01	3.31E+01
10	100	100.15	9.50E-01	1.16E-01	305	166.7	1.46E+00	2.65E+01	3.38E+01
11	110	110.19	1.06E+00	1.24E-01	340	166	1.66E+00	2.71E+01	3.50E+01
12	120	120.18	1.17E+00	1.34E-01	374	166	1.83E+00	2.68E+01	3.58E+01
13	130	130.16	1.29E+00	1.42E-01	409	165.3	1.99E+00	2.70E+01	3.65E+01
14	140	140.14	1.44E+00	1.49E-01	444	165	2.16E+00	2.65E+01	3.74E+01
15	150	150.14	1.82E+00	1.56E-01	479	165	2.34E+00	2.70E+01	3.83E+01

Table C.4: Experimental data for contact resistance test with rough and rusted iron surface at 15 ksi external pressure

S. No.	VOLTAGE TO UPC	I/P VOLTAGE	I/P CURRENT	O/P VOLTAGE	O/P CURRENT	PHASE DIFF	O/P CT VOLTAGE	TEMP1	TEMP2
EXPERIMENT SET 4: 82.7 KIPS FORCE APPLIED, AMBIENT 22.1 DEG C, HUMIDITY 59% (OUTSIDE THE LAB),									
(ALL VOLTAGES IN VOLTS, CURRENTS IN AMPS, ANGLES IN DEGREES AND TEMPERATURES IN DEG C)									
1	10	10.15	0.117	8.40E-03	33.9	157	0.17	27.8	34.4
2	20	20.15	2.11E-01	1.76E-02	63.7	156	3.10E-01	2.71E+01	3.42E+01
3	30	30.135	3.03E-01	2.84E-02	93	159	4.00E-01	2.80E+01	3.42E+01
4	40	40.14	4.00E-01	3.88E-02	123	159	6.12E-01	2.81E+01	3.41E+01
5	50	50.1	4.95E-01	4.89E-02	153.6	1.60E+02	7.68E-01	2.81E+01	3.41E+01
6	60	60.13	5.95E-01	5.86E-02	185.1	161	9.30E-01	2.75E+01	3.43E+01
7	70	70.14	6.97E-01	6.80E-02	223	161	1.08E+00	2.76E+01	3.44E+01
8	80	80.13	8.00E-01	7.72E-02	257	1.61E+02	1.25E+00	2.82E+01	3.46E+01
9	90	90.13	9.04E-01	8.60E-02	290	162	1.42E+00	2.83E+01	3.50E+01
10	100	100.15	1.01E+00	9.44E-02	325	163	1.58E+00	2.70E+01	3.54E+01
11	110	110.29	1.12E+00	1.02E-01	360	162.7	1.74E+00	2.82E+01	3.59E+01
12	120	120.18	1.23E+00	1.09E-01	395	164	1.91E+00	2.80E+01	3.66E+01
13	130	130.16	1.36E+00	1.17E-01	430	164	2.08E+00	2.80E+01	3.74E+01
14	140	140.15	1.50E+00	1.24E-01	464	162	2.24E+00	2.81E+01	3.81E+01
15	150	150.12	1.89E+00	1.31E-01	500	162	2.42E+00	2.83E+01	3.90E+01
16	153	153.12	2.45	1.33E-01	511	161	2.455	28.8	40.1

Table C.5: Experimental data for contact resistance test with rough and rusted iron surface at 20 ksi external pressure

S. No.	VOLTAGE TO UPC	I/P VOLTAGE	I/P CURRENT	O/P VOLTAGE	O/P CURRENT	PHASE DIFF	O/P CURRENT VOLTAGE	TEMP1	TEMP2
EXPERIMENT SET 5: 110.2 KIPS FORCE APPLIED, AMBIENT 22.1 DEG C, HUMIDITY 59% (OUTSIDE THE LAB),									
(ALL VOLTAGES IN VOLTS, CURRENTS IN AMPS, ANGLES IN DEGREES AND TEMPERATURES IN DEG C)									
1	10	low signal							
2	20	20.14	2.14E-01	1.63E-02	64.6	155	3.15E-01	2.92E+01	3.66E+01
3	30	30.12	3.10E-01	2.56E-02	95	155	4.70E-01	2.93E+01	3.66E+01
4	40	40.1	4.06E-01	3.51E-02	125.4	157.7	6.24E-01	2.96E+01	3.64E+01
5	50	50.07	5.05E-01	4.44E-02	156.7	1.59E+02	7.84E-01	2.83E+01	3.64E+01
6	60	60.1	6.06E-01	5.33E-02	188.7	160	9.45E-01	2.87E+01	3.65E+01
7	70	70.12	7.10E-01	6.19E-02	228	160	1.10E+00	2.82E+01	3.66E+01
8	80	80.1	8.14E-01	7.02E-02	261	160	1.27E+00	2.85E+01	3.68E+01
9	90	90.11	9.20E-01	7.80E-02	296	161	1.44E+00	2.98E+01	3.69E+01
10	100	100.13	1.03E+00	8.58E-02	331	160	1.62E+00	2.88E+01	3.73E+01
11	110	110.16	1.14E+00	9.22E-02	366	160	1.77E+00	2.90E+01	3.78E+01
12	120	120.16	1.25E+00	9.92E-02	401	160.3	1.94E+00	2.95E+01	3.84E+01
13	130	130.13	1.38E+00	1.06E-01	437	162	2.11E+00	2.96E+01	3.88E+01
14	140	140.12	1.52E+00	1.13E-01	473	161	2.20E+00	3.00E+01	3.93E+01
15	150	150.11	1.92E+00	1.20E-01	510	161.2	2.48E+00	3.00E+01	4.05E+01

APPENDIX D

PYFLUX CODE FOR SIMULATION

```
#! Flux3D 12.1


lastInstance = SensorPredefinedLosses(name='Sensor_Losses',support=
    ComputationSupportLossesVolumeRegion(region=[RegionVolume['CONTACT'],
    RegionVolume['CONTACT2']]))

lastInstance = SensorPredefinedLosses(name='SENSOR_LOSSES_contact', support=
    ComputationSupportLossesVolumeRegion(region=[RegionVolume['CONTACT']]))

lastInstance = SensorIntegralFace(name='SENSOR_current_contact_s1',
                 spatialFormula='j',
                 support=SupportIntegralFace(faces=[Face[99],
                                                    Face[115],
                                                    Face[119],
                                                    Face[123],
                                                    Face[127],
                                                    Face[133],
                                                    Face[139],
                                                    Face[107]],
                              regionVolume='CONTACT'))

lastInstance = SensorIntegralFace(name='SENSOR_CURRENT_CONTACT_S2',
                 spatialFormula='j',
                 support=SupportIntegralFace(faces=[Face[232],
                                                    Face[240],
                                                    Face[242],
                                                    Face[244],
                                                    Face[246],
                                                    Face[249],
                                                    Face[252],
                                                    Face[236]],
                              regionVolume='CONTACT'))

lastInstance = SensorIntegralFace(name='SENSOR_CURRENT_CONTACT2',
                 spatialFormula='j',
                 support=SupportIntegralFace(faces=[Face[145]],
                              regionVolume='CONTACT2'))

lastInstance = SensorPredefinedLosses(name='SENSOR_losses_CONTACT2', support
    =ComputationSupportLossesVolumeRegion(region=[RegionVolume['CONTACT2']])
    )
```

```
evaluateSensors ()

EvolutiveCurve2D (name='Losses2 ',  evolutivePath=EvolutivePath ( parameterSet =[
    SetParameterXVariable ( paramEvol=VariationParameter [ 'TIME'] ,
formula =['SENSOR_LOSSES ',
        'SENSOR_LOSSES_CONTACT ',
        'SENSOR_LOSSES_CONTACT2 '])

EvolutiveCurve2D (name='EvolutiveCurve2D_32 ', evolutivePath=EvolutivePath (
    parameterSet =[SetParameterXVariable ( paramEvol=VariationParameter [ 'TIME'
    ] ,
formula =['Comp( 3 ,SENSOR_CURRENT_CONTACT2) ',
        'Comp( 3 ,SENSOR_CURRENT_CONTACT_S1) ',
        'Comp( 3 ,SENSOR_CURRENT_CONTACT_S2) '])

lastInstance = VariationParameterFormula (name='Current ',  formula='Comp( 3 ,
    SENSOR_CURRENT_CONTACT2)+Comp( 3 ,SENSOR_CURRENT_CONTACT_S1) ')

EvolutiveCurve2D (name='EvolutiveCurve2D_41 ', evolutivePath=EvolutivePath (
    parameterSet =[SetParameterXVariable ( paramEvol=VariationParameter [ 'TIME'
    ] ,
formula =['current '])

lastInstance = VariationParameterFormula (name='voltage ',  formula='
    SENSOR_LOSSES/ current ')

EvolutiveCurve2D (name='Contact_voltage1 ', evolutivePath=EvolutivePath (
    parameterSet =[SetParameterXVariable ( paramEvol=VariationParameter [ 'TIME'
    ] ,
formula =['voltage '])

lastInstance = VariationParameterFormula (name='IC2 ',  formula='
    SENSOR_CURRENT_CONTACT2')

VariationParameter [ 'IC2 '] . formula='Comp( 3 ,SENSOR_CURRENT_CONTACT2) '

lastInstance = VariationParameterFormula (name='vc2 ',  formula='
    SENSOR_LOSSES_CONTACT2/ ic2 ')

EvolutiveCurve2D (name='EvolutiveCurve2D_71 ', evolutivePath=EvolutivePath (
    parameterSet =[SetParameterXVariable ( paramEvol=VariationParameter [ 'TIME'
    ] ,
formula =['vc2 ',
        'ic2 '])
```

voltage_contact.py

REFERENCES

[1] G. Klempner and I. Kerszenbaum, *Handbook of Large Turbo-Generator Operation and Maintenance.* John Wiley & Sons, 2011, vol. 38.

[2] "Risk-informed inspection of 18mn-18cr generator retaining rings," Electric Power Research Institute (EPRI), Tech. Rep. 3002003589, Nov. 2014.

[3] "Review of damage to generator retaining rings," Electric Power Research Institute (EPRI), Tech. Rep. 3002006238, Dec. 2015.

[4] Wikipedia, "Paschen's law — wikipedia, the free encyclopedia," 2016, [accessed 2-April-2016]. [Online]. Available: "https://en.wikipedia.org/w/index.php?title=Paschen%27s_law&oldid=705254800"

[5] "Paschen curve: Voltage breakdown vs pressure," High Voltage Connection, [accessed 2-April-2016]. [Online]. Available: http://www.highvoltageconnection.com/articles/paschen-curve.html

[6] "Negative sequence effects on generator rotors," Electric Power Research Institute (EPRI), Tech. Rep. 1015671, Jan. 2009.

[7] "Negative sequence effects on generator rotors," Electric Power Research Institute (EPRI), Tech. Rep. 1014910, Dec. 2007.

[8] J. G. Michopoulos, M. Young, and A. Iliopoulos, "A multiphysics theory for the static contact of deformable conductors with fractal rough surfaces," *Plasma Science, IEEE Transactions on*, vol. 43, no. 5, pp. 1597–1610, 2015.